Thesis for the degree of Doctor of Philosophy

Structure and Dynamics in Liquid Battery Electrolytes

Gustav Åvall

CHALMERS

Department of Physics
Chalmers University of Technology
Göteborg, Sweden 2020

Structure and Dynamics in Liquid Battery Electrolytes
Gustav Åvall
ISBN 971-91-7905-247-8.

Doktorsavhandlingar vid Chalmers tekniska högskola
Ny serie nr 4714
ISSN 0346-718X

Department of Physics
Chalmers University of Technology
SE-41296 Göteborg
Sweden

Cover: Artistic rendering of $LiPF_6$ in PC, made with the Deep Dream Generator.

Chalmers, Reproservice
Göteborg, Sweden 2020

Structure and Dynamics in Liquid Battery Electrolytes

Gustav Åvall
Department of Physics
Chalmers University of Technology
SE-41296 Göteborg, Sweden

Abstract

The introduction of Sony's rechargeable lithium-ion battery in 1991 sparked a transformation of our everyday life, enabling wide-spread use of portable electronics, such as smartphones and laptops. Furthermore, in recent years the increased usage of electrical vehicles and the on-going change to transient renewable energy sources has created a large interest in cheaper, safer, more sustainable, long-lasting and energy denser batteries. Next generation batteries – batteries beyond the traditional lithium-ion battery chemistries – offers possible routes towards the for-mentioned sought performance, societal and economical improvements. In this thesis several next generation battery concepts are studied. In particular, *i)* the sodium-ion battery, offering similar energy densities to that of the modern-day lithium-ion battery, but showing better power performance, is cheaper, more sustainable and safer, and *ii)* highly concentrated electrolytes, enabling higher energy densities, improved safety features, and improved cycling stability, are studied.

Several of the improvements in safety and performance seen in these next generation battery technologies stem from the local environment in the electrolyte. In this work I present a comprehensive study of the local cationic environment in several next generation battery electrolytes employing computational methods such as semi-empirical methods, density functional theory, and *ab initio* molecular dynamics. Furthermore, novel methods for studying the dynamics of the solvation shell are presented. The results of these studies are compared to what I and others have found in conventional lithium-ion battery electrolytes, and the connection between the local electrolyte structure and dynamics and the macroscopic electrolyte and battery properties is discussed.

Keywords: lithium-ion battery, sodium-ion battery, highly concentrated electrolyte, DFT, AIMD, ligand-exchange, solvation shell.

List of Publications

This thesis is based on the work contained in the following papers:

I. Solvation structure in dilute to highly concentrated electrolytes for lithium-ion and sodium-ion batteries
E. Flores, G. Åvall, S. Jeschke, and P. Johansson
Electrochim. Acta ***2017****, 233, 134.* DOI: https://doi.org/10.1016/j.electacta.2017.03.031

II. Sodium-ion Battery Electrolytes: Modeling and Simulations
G. Åvall, J. Mindemark, D. Brandell, and P. Johansson
Adv. Energy Mater. ***2018****, 1703036.* DOI: https://doi.org/10.1002/aenm.201703036

III. Li Salt Anion Effect on O_2 Solubility in an Li-O_2 Battery
J. Lindberg, B. Endrődi, G. Åvall, P. Johansson, A. Cornell, G. Lindbergh
J. Phys. Chem. C ***2018****, 122, 4, 1913-1920*. DOI: https://doi.org/10.1021/acs.jpcc.7b09218

IV. Highly concentrated electrolytes: Detailed analysis of the solvation structure of LiPF6 in propylene carbonate lithium-ion battery electrolytes
G. Åvall, J. Wallenstein, G. Cheng, P. Johansson, D. Abraham
Prepared for submission – J. Phys. Chem. C

V. A Novel Approach to Ligand-exchange Rates Applied to Lithium-ion Battery and Sodium-ion Battery Electrolytes
G. Åvall, and P. Johansson
Submitted – J. Chem. Phys.

Contribution Report

I. I performed the computations, suggested the variance as a measure of disorder, analysed the data along with co-authors, co-authored the main part of the manuscript with Eibar Flores.

II. I wrote the liquid electrolyte part of the review.

III. I performed and authored the computational part of the study and manuscript.

IV. I performed the computations, analysed the computational data and carried out parts of the spectroscopic data analysis. I did the comparison of the computational and spectroscopy results. I authored the majority of the paper.

V. I designed the study, developed the new technique of computing ligand-exchange rates, performed the computations, analysed the data, and was the main author of the paper.

List of Acronyms

ACN	Acetonitrile
AIMD	*Ab initio* molecular dynamics
CEI	Cathode electrolyte interphase
CIP	Contact ion pair
CN	Coordination number
CPMD	Car-Parrinello molecular dynamics
DFT	Density functional theory
DMC	Dimethyl carbonate
DME	Diethyl carbonate
EC	Ethylene carbonate
EMC	Ethylmethyl carbonate
ESW	Electrochemical stability window
EV	Electrical vehicle
HCE	Highly concentrated electrolyte
HOMO	Highest occupied molecular orbital
LCO	Lithium cobalt oxide
LFP	Lithium iron phosphate
LIB	Lithium-ion battery
LMO	Lithium manganese oxide
LUMO	Lowest unoccupied molecular orbital
MD	Molecular dynamics
NCA	Nickel cobalt aluminium
NDDO	Neglect of diatomic differential overlap
NMC	Nickel manganese cobalt
PC	Propylene carbonate
PES	Potential energy surface
PM7	Parametrized method 7
RDF	Radial distribution function
SCF	Self-consistent field
SEI	Solid electrolyte interphase
SIB	Sodium-ion battery
SN	Solvation number
SSIP	Solvent separated ion pair
TFSI	Bis(trifluoromethanesulfonyl)imide
VC	Vinyl carbonate

Table of Contents

1. Introduction

In 1991 Sony commercialized its rechargeable lithium-ion battery (LIB), transforming society and our everyday life. The energy density of 200 Wh/l, or 80 Wh/kg, of Sony's original battery made wide-spread usage of portable electronics possible. Since then several types of LIBs have been developed, and the energy densities rapidly increased, having more than tripled [1]–[3], and the use of smartphones and laptops has become second nature to a substantial part of the global population. In 2019, the global sales of LIBs reached more than 316 GWh, with an exponentially increasing trend [4], [5]. The vast majority of LIBs are produced in Asia, but the share of production in Europa and North America is expected to rise [5]. Moreover, the price per kWh is decreasing rapidly for all major types of LIBs [5]. For instance, the price of a battery pack designed for electrical vehicles (EVs) was about 200 €/kWh in 2017 and is expected to be halved, even in the most pessimistic projection, by 2030 [5]. However, there is some uncertainty in the long-term availability of, mainly, lithium and cobalt – a costly metal often used in the cathode in LIBs. Neither lithium nor cobalt are abundant in the Earth's crust. Moreover, the production of lithium and cobalt is dependent on mining of other materials. More than half of annual lithium production comes as a by-product of, mostly, potassium production, and more than 85% of cobalt as by-products in nickel and copper mining [6], [7]. Furthermore, much of the known reserves of these metals are located in geopolitically unstable regions in South America and Africa, often in areas with extreme climate conditions, and has a history of being mined under poor circumstances [8], [9]. Therefore, the prices of these materials can be quite volatile, and although the future supply of lithium seems at present to be accommodated by annual production, the projected need of cobalt for battery applications is more than twice the known global cobalt reserve by 2040 [6], [7].

While the early market for LIBs was portable electronics, today there is a large emphasis on mitigating the effects of climate change and transitioning into a CO_2 neutral society. In the pursuit of lowering carbon emissions, several sectors have identified batteries as promising in the replacement of current high emissive technologies or becoming a part of new energy infrastructure. The transport sector stands for *ca.* 20% of global CO_2 emissions, Figure 1.1, replacing the fossil-fuel powered internal combustion engine with an electrical engine powered by batteries would substantially reduce these emissions [10]–[12]. Furthermore, the emissions from EVs can be reduced even further if both the country where the battery is produced, and where the battery is subsequently charged, has a clean energy mixture [13]–[16]. For a clean energy mix, fossil-fuel power needs to be replaced by CO_2 neutral energy

sources, such as wind, solar, nuclear, hydro and geothermal power. However, energy production from solar and wind power is highly irregular, and hence there is a need for large scale grid energy storage. Due to the role batteries can play in large scale grid storage the World Economic Forum ranked next generation batteries – batteries beyond the traditional LIB chemistries – as the second most important emerging technology in 2016 [17], [18].

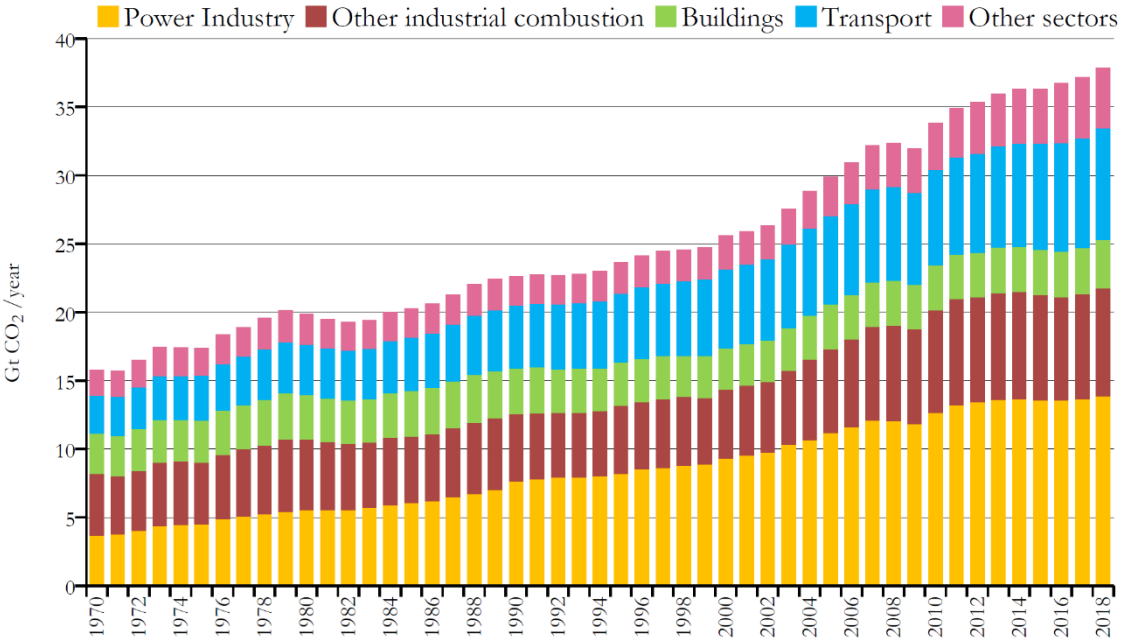

Figure 1.1: Global CO_2 emissions by sector [12].

Alongside batteries fuel cells, supercapacitors and hybrid supercapacitors have all been suggested for EV and grid applications. Supercapacitors and hybrid supercapacitors show an incredible cycle life ($10^5 - 10^6$ cycles for supercapacitors, 10^3 cycles for batteries) and power performance ($10^2 - 10^4$ W/kg for supercapacitors *vs.* 10^2 W/kg for batteries); however, the energy density of these systems are one to two orders of magnitude lower than modern LIBs [19]. Fuel cells have long been studied, showing energy densities several orders of magnitude above modern LIBs within their cells – not at systems level – but due to the needed production of liquid or highly pressurized hydrogen fuel cells are a factor of 3 – 4 times as energy inefficient compared to LIBs [20], [21].

With the transport market and large scale grid storage in mind, the demands on batteries have grown, and each application has its own needs and priorities. EVs need batteries that are safe and reliable, have a high volumetric energy density – to improve drive range – and long cycle life, such that the performance of the EV is stable over time, and the cost over the EVs

lifetime is kept at a minimum. Moreover, even if most of the charging of EVs is done at home or work, fast charging capabilities are sought after such that long pauses are not required on lengthy trips. The cost of the battery is also of importance, as well as the operating temperature range of the battery. In grid storage applications the cost, reliability and cycle life of the battery is of greatest importance, enabling an economic and stable infrastructure component. There is also a general interest in using more abundant materials, moving away from elements such as cobalt.

To meet future demands and tailored needs of each application not only improvements to existing LIB technology are pursued. Several types of next generation batteries have been studied as possible replacements or supplements to LIBs. Among next generation batteries, the sodium-ion battery (SIB) concept overall shows comparable performance levels to LIBs [6], [22]–[25]. Moreover, SIB chemistries are often composed exclusively of abundant materials, although vanadium is seen in some cathodes, and are completely free from lithium and cobalt, and hence SIBs are often cheaper, more sustainable, and less susceptible to fluctuation in prices of raw materials than LIBs [6]. SIBs also displays improved safety, especially during transport, as the battery can be kept in a completely discharged state due to having dual Al current collectors, and has been suggested as a candidate for grid storage [24]–[27].

Recently, highly concentrated electrolytes (HCEs) have been investigated, both for LIBs and next generation batteries. These electrolytes have a salt concentration substantially higher than the conventional LIB electrolyte. They show a wider electrochemical stability window (ESW), enabling cycling at higher voltages, are generally less volatile and have improved power densities due to an increased amount of charge carriers and faster kinetics. However, HCEs are costly and display a decrease in ionic conductivity. Although the ionic conductivity drops when increasing the salt concentration beyond conventional levels, the concentration of charge carriers is higher and the cationic conductivity is not as affected, and hence the cationic transport mechanism in these electrolytes is of scientific interest [28], [29].

Several of the properties seen in HCEs, as well as some differences between SIBs and LIBs, are thought to arise due to the local structure and dynamics of the electrolyte. Improvements in power performance are thought to be connected with the easy at which the cation can desolvate. Similarly, the changes in transport properties seen at elevated salt concentrations are thought to be connected with the stability of the cations solvation shell – a shell of solvents and anions surrounding the cation – and the widening of the ESW has been

discussed in terms of shifts in the molecular orbitals of the solvents upon interacting with a cation [29], [30].

However, synthesising and characterizing novel battery materials is often a costly and time-consuming endeavour. Computational studies offer an alternative and complementary research route, enabling insight into the fundamental processes occurring during battery operation. Properties which are difficult to measure, can often be easily obtain by computations, such as energetically stable solvation shells, or the molecular orbitals of solvents and anions which gives insight into the ESW window of the electrolyte or can be related to decomposition reactions occurring at the electrodes. Frequency calculations can be used as a complement to spectroscopic techniques in order to reveal what bonds are involved in the observed vibrational modes. It also reveals the intensity or activity of the vibrational modes which can be crucial when determining concentrations of certain species in electrolytes from spectroscopic data. Questions regarding transport mechanisms can be hard to address experimentally but can be examined using computations.

1.1 Scope of Thesis

In this thesis, several electrolytes for LIBs and next generation batteries are studied, mainly through computational means, with an emphasis on the effects of the salt concentration on the local electrolyte structure, the dynamics of the solvation shell and interactions among the electrolyte species. The Parametrized Method 7 (PM7), as well as Car-Parrinello molecular dynamics (CPMD) is used to study the local electrolyte structure and dynamics in electrolytes composed of lithium/sodium hexafluorophosphate ($Li/NaPF_6$) in propylene carbonate (PC) or acetonitrile (ACN). Moreover, density functional theory (DFT) calculations are used to probe interactions between electrolyte species, as well as energetically stable and favourable structures in several electrolytes. Finally, the local dynamics of the solvation shell is investigated through several methods, including new approaches to studying the forces and velocities on the constituents of the solvation shell and a novel method enabling the direct computation of the ligand-exchange rate from *ab initio* molecular dynamics (AIMD) is presented. Previously, the ligand-exchange rate was, with very few exceptions, calculated using classical molecular dynamics (MD) due to the need for large systems sizes and long trajectories to gather statistics on ligand-exchanges. However, classical force-fields are often ill-equipped to accurately model the strongly ionic environment of HCEs. The new method relies on analysing average velocities on solvent molecules and radial distributions functions, making it feasible to study ligand-exchange phenomenon through *ab initio* methods.

2. Batteries

2.1 Electrochemistry and Applications

In essence, a battery is an electrochemical device able to store chemical energy and convert it into electrical energy through redox reactions. The heart of the battery is the electrochemical cell, and the chemistry of this electrochemical cell ultimately determines the performance of the battery. The electrochemical cell is composed of four main components: Two electrodes, *i)* The cathode, where reduction occurs during discharge, *ii)* The anode, where oxidation occurs during discharge, *iii)* The electrolyte, through which ionic species migrate between the electrodes, and *iv)* The separator, that hosts the electrolyte and hinders the electrodes from short-circuiting by preventing them from coming in direct physical contact. Along with these components, current collectors, composed of materials with high electronic conductivity such as thin metal foils, connects the electrodes with an external circuit. During operation ions travel between the electrodes through the electrolyte. Upon reaching the electrodes they undergo reduction/oxidation reactions with the electrode materials. As a consequence, a current of electrons flows between the electrodes through the current collectors and the external circuit where work can be exerted (Figure 2.1).

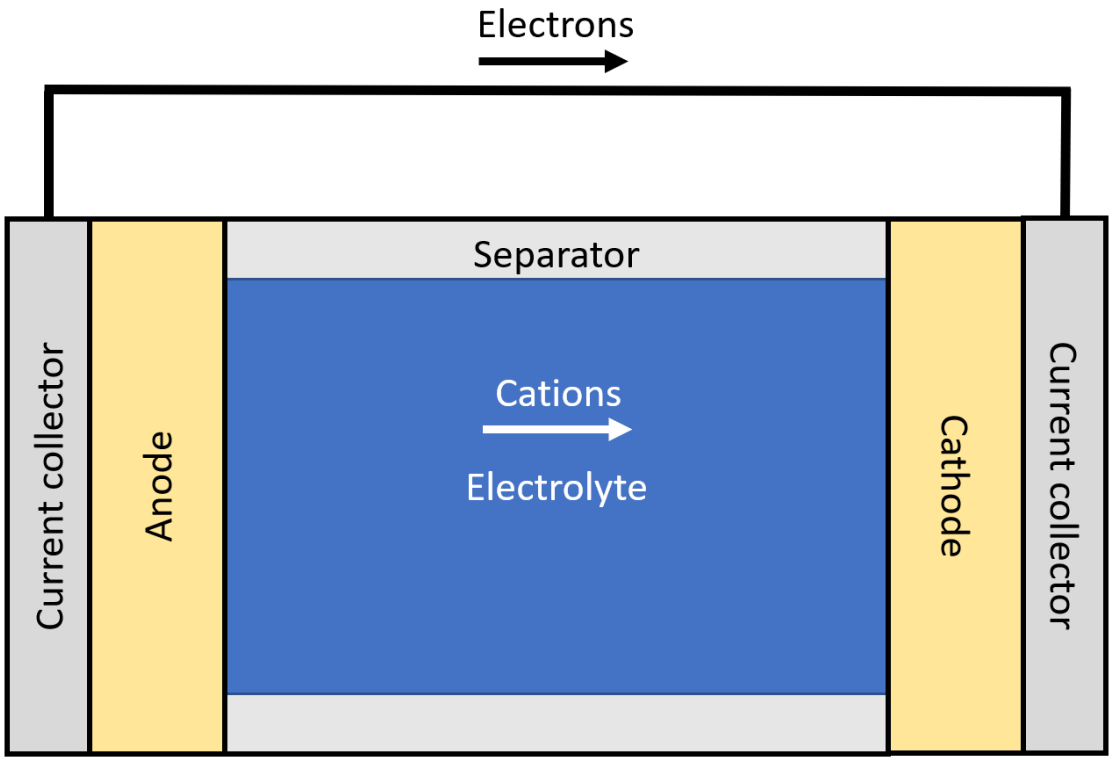

Figure 2.1. Sketch of a modern battery during discharge.

The battery either contains a single electrochemical cell, or several connected in series or parallel depending on the application. A casing for the cells ensures the structural stability of the cell and protects the electrodes and the electrolyte from the environment. Moreover, the battery can contain electrical and thermal control units for the electrochemical cells, and, finally, housing for all the components.

The cathode and anode store the species undergoing redox reactions, and thus effectively store the energy. In LIBs, the cathode and anodes store the lithium-ions and allow them to be reversibly inserted/extracted from the electrodes. In a LIB (Figure 2.2), with a graphite anode and an $LiCoO_2$ (LCO) cathode, the ideal discharge reactions would be:

Oxidation at anode: $LiC_6 \rightarrow C_6 + Li^+ + e^-$

Reduction at cathode: $Li^+ + e^- + CoO_2 \rightarrow LiCoO_2$

Total Reaction: $LiC_6 + CoO_2 \rightarrow C_6 + LiCoO_2$

The amount of lithium that the electrodes can support will ultimately determine how many redox reactions can occur, and thus ultimately how much energy can be stored and subsequently converted back to electrical energy. The amount of lithium, or other relevant species, that an electrode material can store, and use for redox reactions, is given by the capacity Q. The capacity can simply be increased by increasing the amount of electrode materials, thus the specific capacity C – capacity per electrode mass – is of more practical significance. The theoretical specific capacity C_{th} of the electrodes, computed in the discharged state, can be determined using Faraday's law

$$C_{th} = \frac{nF_0}{M_W},$$

were n is the number of electrons transferred in the oxidation/reduction reaction, F_0 is Faraday's constant and M_W is the molecular weight of the electrode material. For example, in the graphite anode of a LIB there is six carbon atoms per lithium, the molecular weight of graphite is 12.011 g/mol, and one electron is transferred during oxidation, yielding a theoretical specific capacity of 372 mAh/g. Similarly, the molar mass of LCO is 97.87 g/mol, again there is only one electron transferred during reduction, yielding a theoretical specific capacity of 274 mAh/g. The actual specific capacity of the system is limited by the theoretical specific capacity.

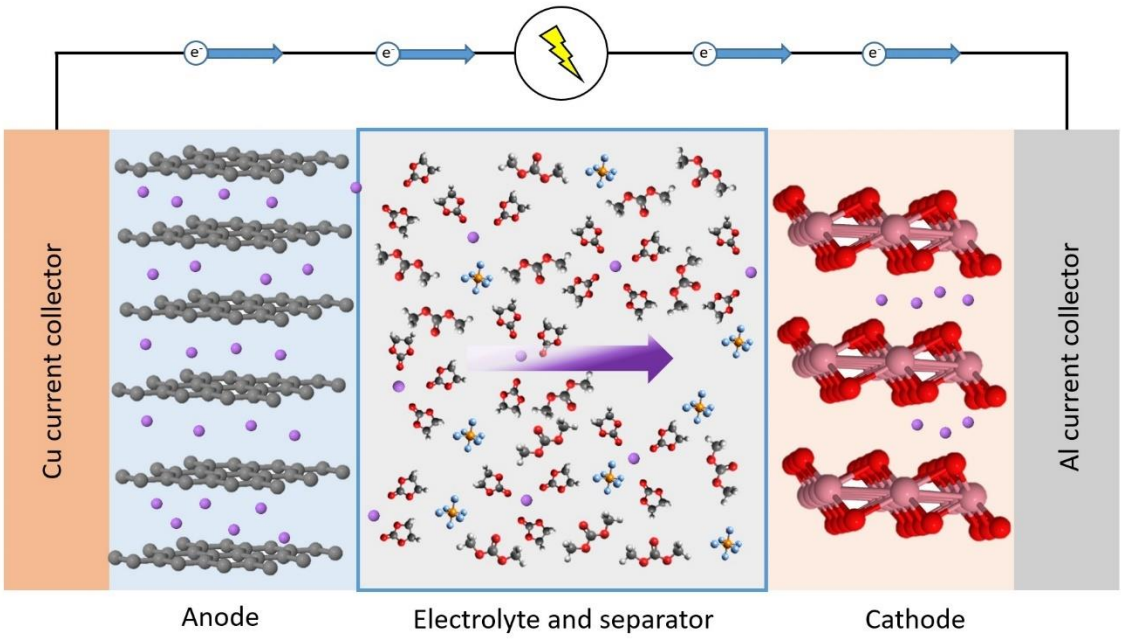

Figure 2.2: A schematic view of a LIB during discharge. Li^+ (purple) moves from the anode to the cathode through the electrolyte, while electrons move in an external circuit.

The redox reactions taking place at the electrodes determines the theoretical voltage, V_{cell}. If the redox reactions are known the Gibbs free energy of the reactions can be calculated [31]. The change in Gibbs free energy ΔG can then be related to the theoretical voltage of the cell through Nernst equation:

$$V_{cell} = -\frac{\Delta G}{nF_0}.$$

The theoretical voltage sets an upper limit for the actual voltage *V,* which is given as the difference in potential between the cathode and anode

$$V = E_{cathode} - E_{anode},$$

and varies during charge/discharge. Hence, the voltage depends on the amount of charge – the state of charge – *q,* that has been transferred between the electrodes, *V=V(q)*. The cell chemistry determines how the voltage depends on *q*, but in general there are three types of voltage profiles: *i)* A flat profile, where the voltage is largely constant during discharge, *ii)* A multi-step profile, displaying multiple plateaus, and *iii)* A sloping profile where the voltage steadily decreases during discharge (Figure 2.3).

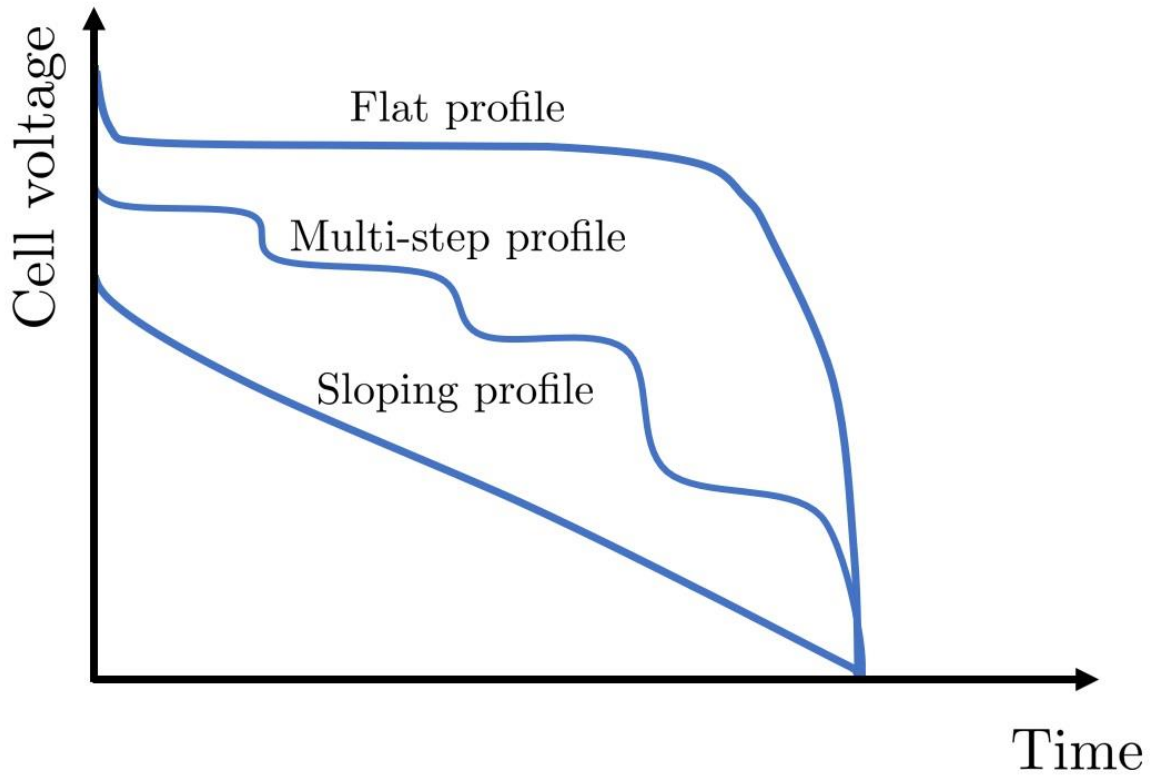

Figure 2.3. The three types of voltage profiles.

The profiles are directly related to the processes taking place in the battery. A flat profile, or a plateau shows that there is an equilibrium between two phases. For instance, during charging, lithium-ions starts to intercalate and pack into graphite in multiple steps, forming LiC_{18}, then LiC_{12}, and finally LiC_6. The voltage profile thus contains multiple steps, and on each plateau two of these phases coexists – but one is converted into the other. Between plateaus, or in sloping profiles, there is only one phase [32]. Moreover, the voltage of the cell must be within the ESW of the electrolyte, otherwise the electrolyte will start to decompose, which can lead to passivation of the electrodes, gas evolutions, irreversible capacity loss, *etc*.
The voltage and capacity of the cell determines the energy of the cell

$$E = \int_0^Q V(q)dq.$$

The gravimetric energy density, or the specific energy, and the volumetric energy density is given by the ratio of the energy and the mass/volume of the cell. Thus, there are two fundamental ways to increase the specific energy of an electrochemical cell: Either increase the density of charges that can be reversibly utilized, *i.e.* the specific capacity, or increase the voltage between the electrodes, which in practice means finding redox reactions that release large amounts of energy. In the case of the previously discussed LIB we found a theoretical

specific capacity of 372 mAh/g for the graphite anode and 274 mAh/g for the LCO cathode. As the theoretical specific capacity of the cathode is lower than the anode, we need more cathode material than anode material to make full use of the capacity in the anode. In this case, we need about 1.4 kg of cathode per kg of anode. The average voltage of a cell with graphite and LCO is 3.8 V [33], yielding a theoretical specific energy of 589 Wh/kg, which is more than double the energy density of a modern day LIB. The discrepancy arises due to several factors. For instance, it is impossible to completely deplete an LCO electrode of lithium without compromising the mechanical stability - only *ca.* 50% of the lithium can be extracted. Additionally, the mass of the electrolyte, separator, current collectors and such, have not been accounted for, *etc*. There is no agreed upon standard for what masses and volumes are accounted for when calculating volumetric and gravimetric energy densities, ranging from only the active material to the fully assembled battery, hence reported gravimetric and volumetric energy and power densities can differ a lot. Modern day LIBs, which are considered to be highly optimized, typically reach around 45% of the theoretical energy density when all parts of the battery is accounted for, *i.e.* including housing, external protective devices, *etc* [34].

The power *P* is determined by how fast the discharge process proceeds. If an amount of charge $\Delta q = q_2 - q_1$ is transferred during a time interval *T* the power is given by the integral

$$P = \frac{1}{T}\int_{q_1}^{q_2} V(q)dq$$

Similarly, the gravimetric and volumetric power density is determined by taking the ratio of the power and mass/volume of the cell. The power of a battery can vary depending on the state of charge. Moreover, there are many factors that determines the power. For instance, the ionic conductivity of the electrolyte sets a limit for how fast ions can be transferred between the electrodes, and the kinetics of the redox reactions themselves can limit the power.

2.2 Lithium-ion Batteries

In 2019 the Nobel prize in chemistry was awarded John B. Goodenough, M. Stanley Whittingham and Akira Yoshino for their contribution in the development of the LIB [35]. Whittingham studied materials, such as TiS_2, with the ability to intercalate and host lithium-ions within their structures [36]. He subsequently went on to propose that such materials could be used as anodes for batteries. This is what is today called insertion/extraction, or simply referred to as intercalation materials. Similarly, in 1979/1980 Goodenough and co-

workers studied layered oxides with the ability to intercalate and store lithium-ions. They discovered that LCO could be used as a cathode material, which is still today one of the most commonly used cathodes in LIBs [37]. In 1980 Michel Armand went on and proposed the rocking-chair concept, where he envisioned a battery where both the anode and cathode participate in the electrochemical reaction through the intercalation mechanism [38], and proposed graphite as an intercalation anode [39]. In 1983 Yoshino and his team put together a rocking-chair type battery that had all the fundamental building blocks of Sony's commercial product, using soft carbon as an anode and LCO as a cathode [40]. Several other important contributions have been made along the way, such as the development of the conventional electrolyte of 1 M $LiPF_6$ in a mixture of ethylene carbonate (EC) along with a linear carbonate, by Tarascon *et al.* [41], which will be covered in detail in Chapter 3. Another important discovery was made by Peled *et al*. [42] – the solid electrolyte interphase (SEI). The operating voltage of the anode in LIBs is within the ESW of the electrolyte, causing reduction of the solvent molecules and ensuing irreversible capacity loss. However, the irreversible capacity loss is only seen during the first few cycles. What Dahn *et al.* discovered was that during these first cycles the reduction products from the electrolyte formed a film on the surface of the anode, the SEI, which is electronically isolating, thus stopping further decomposition of the electrolyte, yet allows Li^+ to diffuse through it [43]. Since then optimizing the formation and subsequent structure of the SEI has been an active research topic [44].

What makes the LIB stand out is the large gravimetric energy density of *ca.* 250 – 300 Wh/kg, and volumetric energy density of *ca*. 600 – 650 Wh/l at the cell level [34], [45], compared to other rechargeable batteries, such as NiCd and NiMH, with densities of *ca*. 100 Wh/kg [46], [47]. Combined with the long cycle life it is the battery of choice for portable electronics [46] and EVs [32], [48].

2.2.1 Anodes

Graphite is still the LIB anode of choice. It reduces lithium at 0.3 V *vs.* Li°/ Li^+, and displays a high specific capacity [1], [49]. Alternatively, lithium titanium oxide $Li_4Ti_5O_{12}$ which reduces lithium at 1.5 V *vs.* Li°/ Li^+ with a negligible effect on the crystal structure upon lithium intercalation can be used. $Li_4Ti_5O_{12}$, however, has a low specific capacity, which along with the relatively high reduction potential yields cells of comparatively low energy densities [50]–[52].

2.2.2 Cathodes

The cathodes found in LIBs are often composed of transition metal compounds. LCO, with its high oxidation potential and relatively large specific capacity, is a commonly used cathode in the majority of smartphone batteries [6]. But, LCO has a modest cycle life (500-1000 cycles) and rather poor thermal stability. $LiNi_xMn_yCo_zO_2$ (NMC) offers 1000-2000 cycles, shows greater thermal stability, and similar energy densities, and is therefore the cathode of choice in EV applications [6]. The properties of NMC can be tuned by changing the ratios of nickel, manganese and cobalt. The most common being the 111 composition, yielding high energy densities, but a lot of research has been put into reducing the cobalt content, developing nickel-rich NMC cathodes, such as NMC(811) [45], [53]. $LiNiCoAlO_2$ (NCA), often with 80% nickel, 15% cobalt, and 5% aluminum, has an energy density of 200 – 250 Wh/kg, and good cyclability (1000 – 1500 full cycles) and was/is used by Tesla in their EVs [54]. The use of cobalt in LCO, NMC, and NCA is a major drawback due to the high toxicity, questions regarding future supply of resources, and the hazardous and poor mining conditions sparks an interest in cobalt free cathodes, such as $LiMnO_2$ (LMO) [6], [8], [9], [55]. Although LIBs using LMO suffer from lower energy densities, they show high power density, good cycle life and thermal stability. LMO based LIBs are primarily used in some EV applications and E-bikes [6]. Finally, $LiFePO_4$ (LFP), also discovered by Goodenough makes for a very stable cathode, showing long cycle life, and makes for a durable and eco-friendly cathode [56].

2.3 Next Generation Batteries

Next generation batteries are batteries that have moved beyond the traditional LIB chemistries. There is a multitude of such batteries being proposed. Starting with the solid-state lithium battery, which uses lithium metal as an anode, and the separator and liquid electrolyte has been replaced by an ionically conductive solid polymer or a ceramic. These batteries are associated with improved safety, operation in a wider temperature range, improved cycle life, and high theoretical specific energy [34]. However, the improved energy density hinges on the replacement of the typical graphite anode in LIBs, by a lithium metal foil [57], [58]. Moreover, the all solid-state battery suffers from slow kinetics, possibly due to high interfacial resistance, possibly due to poor contact between the electrodes and the solid electrolyte, which limits the power density of these systems [57].

Lithium metal anodes can also be balanced by a sulfur conversion electrode, showing a theoretical specific capacity of 1672 mAh/g_{sulfur}, to create a lithium-sulfur battery which promises high gravimetric energy density [34]. The system, however, suffers from severe irreversible capacity losses, related to the solubility of polysulfide species [59].
Another alternative is to use an air, or O_2, cathode – promising extremely high energy densities [60]. The electrolyte, however, is in contact with highly reactive reduced oxygen species, leading to decomposition of the electrolyte and irreversible capacity loss [61], [62]. Another challenge is to design a porous membrane, which allow O_2 from the atmosphere to effectively diffusion though it, while blocking other atmospheric gases [61], [62]. The solubility of O_2 in the electrolyte is directly linked to the capacity of the battery. In **Paper III** the anions effect on O_2 solubility is investigated.
Several battery technologies using multivalent cations have also been proposed. In particular, magnesium, calcium and aluminum metal batteries have gained some interest in recent years. As these are multivalent (Mg^{2+}, Ca^{2+}, and Al^{3+}) the anodes have very high specific capacities, which promises very high energy density systems [63]–[65]. However, there are several technical bottlenecks for these batteries. The metal anodes are highly reactive and passivating films easily form on the metal surfaces, completely disabling the ions from reaching the anode, thus the metal foils need to be produced in extremely clean environments with no traces of oxygen, water, carbon or other contaminants [63][66]. Due to the stiffness of magnesium and calcium, it has also been problematic to create the thin metal foils [63], and it has been difficult to find a suitable cathodes that allows for reversible intercalation of the cations [63][64]. Moreover, the electrochemical reactions in the calcium battery system, just as the LIBs, is SEI controlled, however, it has proved difficult to produce SEIs that conduct Ca^{2+}, and calcium batteries currently have to be cycled at high temperatures (75 – 100°C) to achieve reversibility [65], [67]. Current realised aluminum-ion batteries display a low specific energy (40 Wh/kg) due to Al^{3+} being transported, and intercalated, as a $[AlCl_4]^-$ complex, and hence the cathode needs to be able to accommodate such a large and heavy complex, drastically reducing the energy densities [63].

2.3.1 Sodium-ion Batteries

The first time I encountered sodium for batteries was in Jules Vernes classic *20 000 Leagues under the sea*, from 1870, where Captain Nemo uses sodium batteries to power his submarine Nautilus [68]. The first real world rechargeable SIBs came about at the end of the 1980s and

beginning of 1990s [69], [70]. But as LIBs emerged on the market SIBs were largely forgotten until recently.

Owing to the close chemical resemblance between sodium and lithium, the similarities between SIBs and LIBs are plentiful. Thus, the wealth of knowledge from LIB research, and existing infrastructure, can often be directly applied to SIBs [71]. SIBs offer similar levels of gravimetric energy densities as LIBs, largely owing to the replacement of a Cu current collector by an Al current collector [22], [23], [72], good power densities [22], [26], but lower volumetric energy densities [71]. Moreover, SIBs are often made from abundant materials – with the exception of vanadium, found in some cathode materials – and thus the supply of resources is not at risk, making SIBs cheaper than LIBs [6]. SIBs are considered as candidates for grid energy storage and E-bikes [71], [73].

One major difference between Li^+ and Na^+, is that Na^+ interacts very weakly with graphite, and the structures it forms with graphite are barely energetically stable [74]. Thus, Na^+ does not intercalate well into a graphite anode [75], [76] – although co-intercalation using diglyme based electrolytes is possible [77]. Instead, metal oxides, including several titanium oxides, have been investigated, such as $Na_2Ti_3O_7$, with an insertion potential of 0.3 V [78], but these in general have quite high insertion potentials, resulting in low energy densities [26]. Instead, hard carbon has become the anode of choice in SIBs [79]. Hard carbon is a nano-porous material consisting of disordered stacks of graphene sheets, which readily accepts Na^+ into its structure at a low insertion potential of 0.005 V vs. Na^+/Na, and has a high specific capacity of 300 mAh/g [80]. There are, however, risks of Na-plating and large irreversible capacity losses.

The SIB cathode needs to be able to intercalate Na^+, without large volume expansions. Layered oxides, just as for LIBs, have been studied as possible SIB cathodes [26]. Several of these contain vanadium, such as $NaVPO_4F$ [81], and $Na_3V_2(PO_4)_3$ [82], and have shown promising cyclability and energy densities [26]. To avoid vanadium, Prussian blue analogues and sodium nickel-oxide $NaNi_{(1-x-y-z)}Mn_xMg_yTi_zO_2$ has seen some commercial use in E-bike applications [71]. Several manganese layered oxides have been investigated [83], with full cells showing good cycling stability, high voltages 2.7 – 5 V, and good capacities of *ca.* 190 mAh/g, yielding good energy densities [84], [85].

The electrolytes used in SIBs are to a large extent similar to those found in LIBs, with the sodium analogue of the salt [25] and will be discussed in detail in Chapter 3.

3. Electrolytes

Non-aqueous liquid electrolytes are composed of mixtures of salts and solvents, and the main role is to act as a medium that facilitate transport of ions yet is electronically insulating. The roles the electrolyte must play, however, and the requirements placed upon it are plentiful and many arise due to it being in direct contact with all cell components. Therefore, in order for stable cycling the electrolyte must be chemically and electrochemically stable towards all components of the cell. In general, the operating voltage of the electrochemical cell needs to be within the ESW, defined as the potential window between the highest occupied molecular orbital (HOMO) and lowest unoccupied molecular orbital (LUMO) of the electrolyte (Figure 3.1). In many battery systems, however, such as LIBs and SIBs, the operating voltage is outside the ESW. In such systems, the decomposition products of the electrolyte must form passivating films at the electrode surfaces that allow for reversible cycling. Typically, during the first few cycles of these batteries the products from the reduction of the electrolyte forms the SEI on the anode, and the oxidation products the cathode electrolyte interphase (CEI) on the cathode. These passivate the electrodes, suppressing any further decomposition of the electrolyte, yet allow cations to diffuse through them, allowing continued battery operation (Figure 3.1). Thus, the LIB/SIB electrolytes must either have wide ESWs (3 – 5 V), or the ability to form a stable SEI. Often sacrificial additives are used to form the SEI, the by far most common being vinyl carbonate (VC) which creates a polymeric SEI in EC based electrolytes [86], [87].

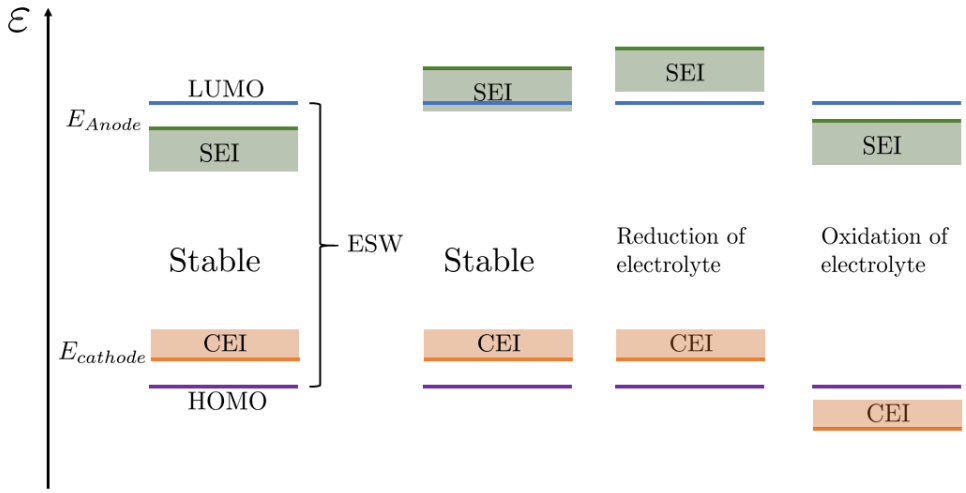

Figure 3.1. Schematic representation of the ESW.

The electrolyte must also allow for fast ion solvation and desolvation, such that the electrochemical cells can charge/discharge at an adequate rate. Similarly, the ionic

conductivity must be high enough (> 1 mS/cm) such that the power density of the cell is sufficient. The electrolyte should also be thermally stable – the melting and boiling points should be outside the internal temperature of the cell during operation and storage, and the flashpoint should be high. Moreover, the electrolyte should have low toxicity, be made of sustainable materials, and have a low production and materials cost.

3.1 The Local Electrolyte Structure

The local electrolyte structure carries importance for many battery properties, having direct implications for the SEI, CEI, conductivity, kinetics, safety and stability of the system [88], [89]. The solvents, although neutral, carry an electromagnetic multipole-moment and hence interact with the cations and anions in the electrolyte. The strong spherically symmetric electric field generated by the cations will align the solvents in its vicinity, thus giving rise to a local structure; the *first solvation shell*, or simply the solvation shell. Beyond the first solvation shell, the second solvation shell is found. Here, the electric field has weakened considerably, however, there is still some structure. Outside the second solvation shell the presence of the cation is hardly noticeable on the solvents (Figure 3.2).

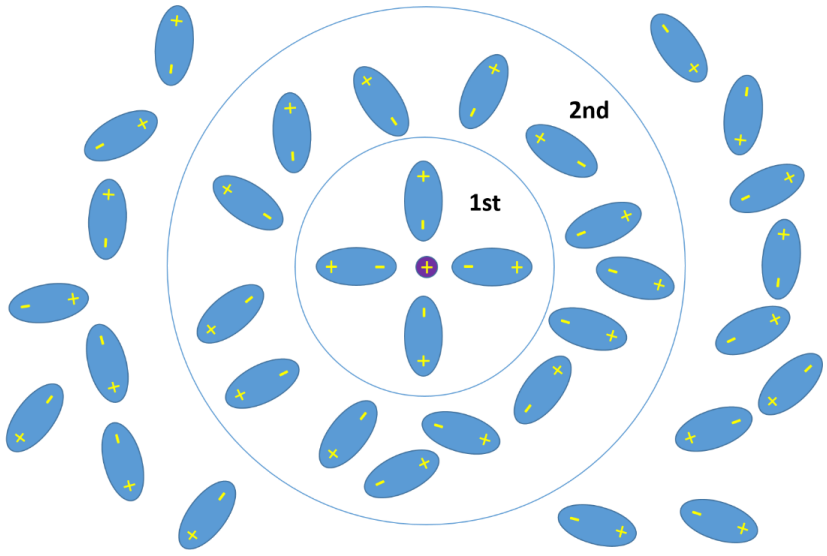

Figure 3.2. Schematic illustration of solvents structured around a cation.

This picture is “accurate” at low salt concentrations, where the average distance between ions is great, however, already at conventional battery electrolyte salt concentration of 1 M the anions has an effect on the cation solvation shells. Anions will be found in the second solvation shell, forming a solvent separated ion pair (SSIP), or even in the first solvation shell, neutralizing the complex and creating a contact ion pair (CIP). Beyond the

conventional salt concentration, the notion of solvation shells break down as large aggregates of ions and solvents start to form (Figure 3.3).

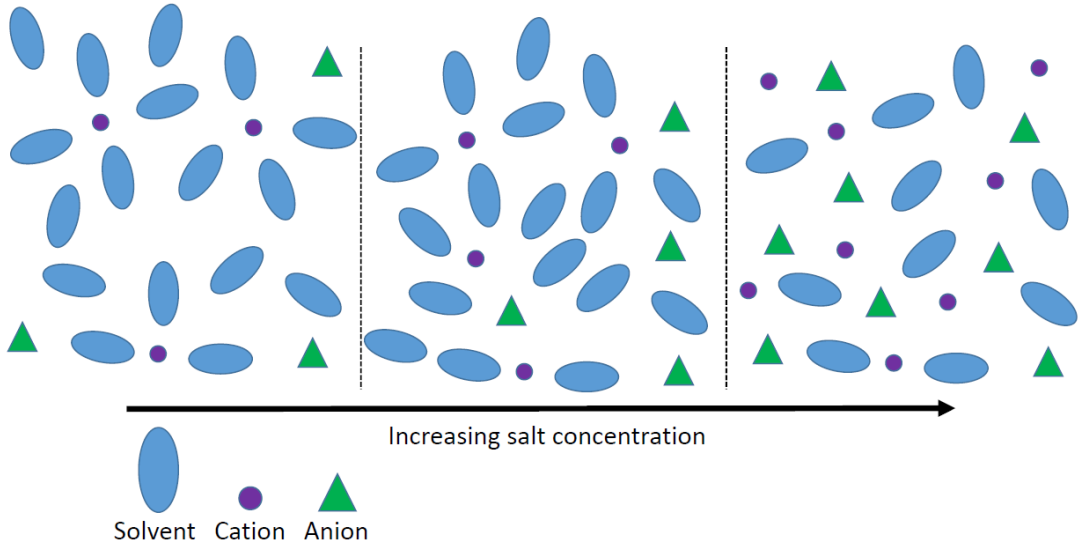

Figure 3.3. The local electrolyte structure as a function of concentration.

There are many ways of investigating the local electrolyte structure. The *radial distributions function* (RDF) – shows the content and size of the solvation shell, or equivalent at high salt concentration. The partial RDF counts the density of an atomic species around the cation:

$$g_i(r) = \frac{n_i(r)}{4\pi r^2 \Delta r} \frac{1}{\rho_i},$$

where ρ_i is the number density of atomic species i, and $n_i(r)$ is the average number of atomic species i within a shell of thickness Δr at distance r from the cation. An RDF typically shows a clear first peak, which defines the size of the first solvation shell (Figure 3.4).

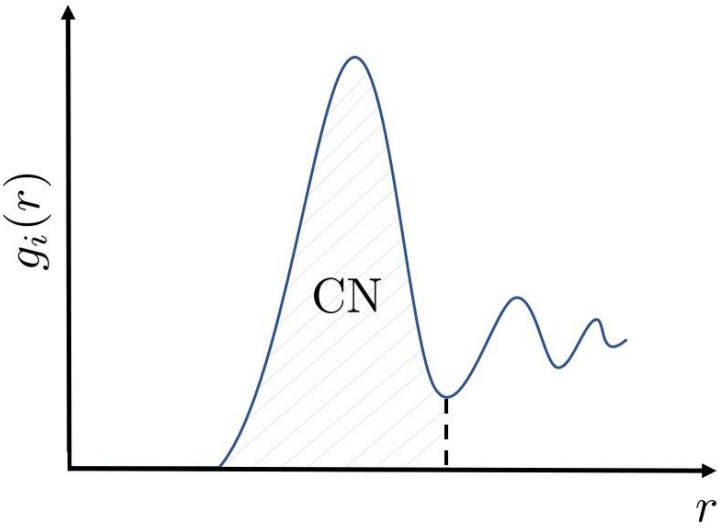

Figure 3.4. Structure of a typical RDF. Shaded area is the CN.

By integrating the partial RDFs the average number of atomic species – the (partial) coordination numbers (CNs) – in the solvation shell can be computed. But, this only yields an average number. The CNs can also be computed by keeping track of all the atomic species *i* within the first solvation shell. A distribution of CNs is thus obtained. The variance of this distribution can be used to quantify the diversity of the local electrolyte structure, *e.g.*, a variance of 0 in all the partial CNs indicate that all the solvation shells are identical, while if the variance of the CNs are high, there are several types of solvation shells, differing in content and possibly structure. The solvation number (SN), however, measures the number of solvents/anions in the solvation shell, and can be computed in a similar fashion as the CN. There are several methods of experimentally determining the CNs/SNs [90] – although it can be ambiguous if it is the CN or SN being measured. Using Raman and IR, the spectrum of the electrolyte, compared with that of a neat solvent, will have shoulders on some of the peaks associated with the solvent (Figure 3.5). Similarly, if the spectrum of an extremely dilute electrolyte is compared with the spectrum of an HCE, one will notice shoulders on peaks associated with the anion in the HCE spectrum. These shoulders arise as the normal modes of the solvents/anions are perturbed by the presence of the cation. Moreover, typically the vibrational modes associated with the bonds to the atomic species directly coordinating the cation are the ones affected.

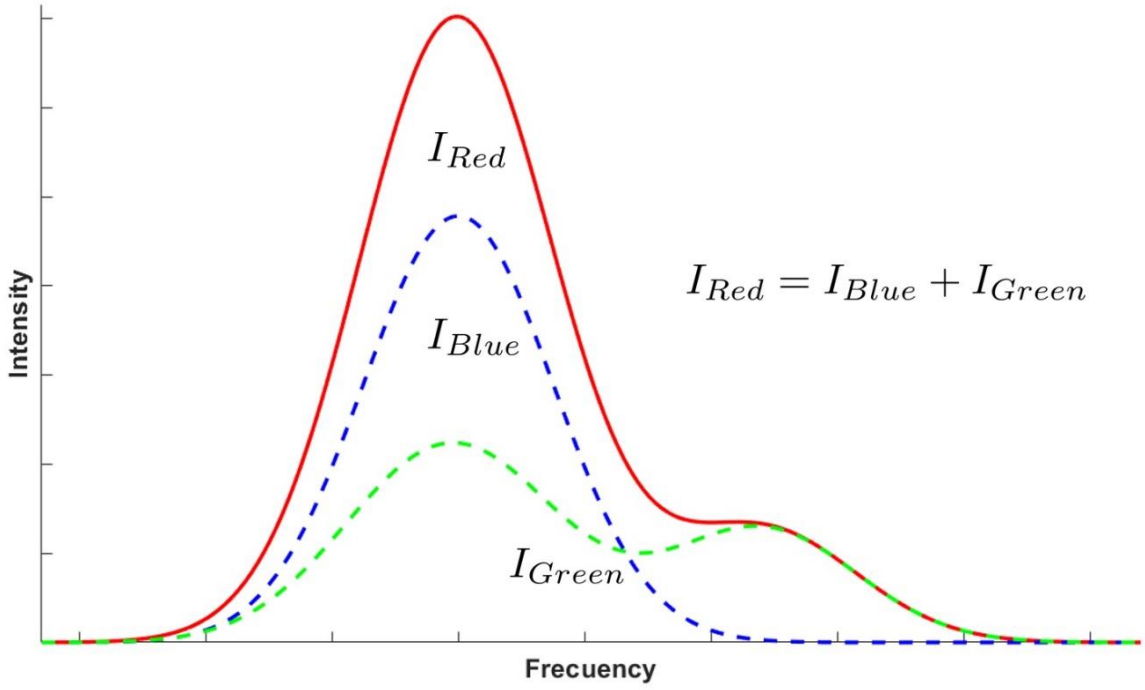

Figure 3.5. The red peak deconvoluted into its two components, blue and green.

By deconvoluting the peaks and comparing the respective integrated intensities the content of the solvation shell can be ascertained. In particular, let c_i denote the concentration of species *i* and $c_{i,coord}$ the concentration of coordinated species *i,* then the fraction of coordinated species *i* can be computed

$$\frac{c_{i,coord}}{c_i} = \frac{I_{i,coord}}{I_{i,coord} + I_{i,free}}$$

where $I_{i,coord}$ and $I_{i,free}$ are the integrated intensity of the peak associated with coordinated and free species *i*, respectively. Note that c_i is known from the preparation of the electrolyte, and hence $c_{i,coord}$ can be determined. The ratio $c_{i,coord}/c_{salt}$ can now be used as a measure of the partial CN/SN. This analysis, however, can become substantially more complicated if the cross section of the vibrational mode is affected by the proximity of the cation. In essence, the integrated intensity is a sum over all oscillators contributing to the specific peak; $\sum \mathrm{a_j} = N_i a_i = I_i$ assuming there are N_i harmonic modes all absorbing/transmitting with the same intensity a_i. Hence

$$\frac{I_{i,coord}}{I_{i,coord} + I_{i,free}} = \frac{N_{i,coord} a_{i,coord}}{N_{i,coord} a_{i,coord} + N_{i,free} a_{i,free}}.$$

which is only equal to $c_{i,coord}/c_i$ if $a_{i,coord} = a_{i,free}$. If this is not the case the observed integrated intensities can be scaled by the intensities a_i:

$$\frac{I_{i,coord}/a_{i,coord}}{I_{i,coord}/a_{i,coord} + I_{i,free}/a_{i,free}} = \frac{I_{i,coord}}{I_{i,coord} + \frac{a_{i,coord}}{a_{i,free}} I_{i,free}} = \frac{N_{i,coord}}{N_{i,coord} + N_{i,free}} = \frac{c_{i,coord}}{c_i}.$$

The intensities a_i are often not substantially affected by the solvent/anion being coordinated to the cation. But, there are important cases, such as in EC and PC based electrolytes, where this procedure is required to get consistent results [91]. In practice, the Raman activities or IR intensities, computed with quantum chemical methods, are used to scale the integrated intensities.

The structure of the solvation shell can be further investigated using MD by computing angles between cations and coordinated atomic species or centre of masses of the solvents. The above-mentioned methods of studying the solvation shell structure and content are used extensively in **Paper I**, **IV**, and **V.**

3.2 Ion Transport

There are two broad categories of transport present in an electrolyte; diffusion, which is transport caused by a concentration gradient, and migration, which is transport of charged species due to an external electric field. In bulk electrolyte, diffusion is the main cause of transport, however, even if the driving force of the transport is known, *i.e.* primarily a concentration gradient, the actual mechanism depends on the composition of the electrolyte. In a battery, the electrodes can be viewed as sources/sinks of cations, and there is generally a higher ionic concentration close to the electrode surfaces, giving rise to a concentration gradient. Diffusion acts to homogenize the concentration, thus without any sources or sinks, diffusions will cease once the concentration is constant. Fick's law governs diffusion, which relates the flux J_i of species i to the gradient of the concentration c_i:

$$J_i = D_i \frac{\partial c_i}{\partial x},$$

where D_i is the diffusion coefficient of the species. As diffusion drives towards removing all concentration gradients, the concentration will change with time. Fick's second law relates the time derivative and Laplacian

$$\frac{\partial c_i}{\partial t} = D_i \frac{\partial^2 c_i}{\partial x^2}.$$

If the first solvation shell is stable, it will diffuse as one large positively charged unit – the vehicular transport mechanism. A sphere moving though a viscous fluid is a simple model of such a system – leading to the Stokes-Einstein relation for the diffusion coefficient

$$D = \frac{k_B T}{6\pi r_s \eta}.$$

where r_s is the size of the solvation shell and η the viscosity of the fluid. It is clear from this that the diffusion coefficient of the cation and anion, D_+ and D_-, differ, as their values of r_s differ. Therefore, the cation and anion contribute inequality to the ionic conductivity. The transport numbers are the fraction of the current carried by the cation and anion respectively:

$$t_+ = \frac{D_+}{D_+ + D_-}, \quad t_- = \frac{D_-}{D_+ + D_-}.$$

The Stokes-Einstein relation, however, is only applicable in very dilute electrolytes where the interactions between ions are negligible. In any electrolyte with a moderate salt concentration the ion-ion interactions must be considered.

If the salt is completely dissociated, the molar conductivity $\Lambda = \sigma/c$, where σ is the ionic conductivity, is given by an expression due to Onsager and Fuoss:

$$\Lambda = \Lambda_0 + Sc^{1/2} + Ec\,log\,c - J_1 c + J_2 c^{3/2}$$

where S, E, J_1 and J_2 are functions that depends on the temperature, dielectric constant, viscosity, the molar conductivity at infinite dilution and the ions closest distance of approach [92]. At high enough salt concentrations, however, ions will start to associate, forming SSIPs, CIPs, and larger aggregates. The closest thing to a theory for transport in such electrolytes is a continuum model by Newman [93]. This model relies on pair wise friction coefficients between the species in the electrolyte. But, no theoretical basis, or origin, is given for these coefficients, and they have to be determined from measurements of the diffusion coefficients, conductivity and transport numbers [93]. Thus, there is no fundamental theory for conductivity in such electrolytes. Several important observations, however, have been made. As there are now CIPs the ionic current is not simply carried by the cation and anion, but also by larger charged complexes. The transference numbers give the fraction of the current carried by the cation and anion, respectively, when CIPs and larger aggregates are present

$$T_+ = \sum_i sgn(q_i) n_i t_i$$

$$T_- = \sum_j sgn(q_j) n_j t_j,$$

where the sum over i and j run over complexes containing cations and anions respectively, q_i and q_j is the total charge of complex i and j, respectively, and n_i and n_j are the number of cations and anions in complex i and j, respectively. The transference/transport number of the cations generally increase with salt concentration [29], and the cations no longer seem to have stable first solvation shells, and the transport mechanism deviate from vehicular transport and grows complex. The exact transport mechanism arising in these HCEs is still under debate, and hopping through ligand-exchange has been suggested as a possible mechanism [94]–[100], and/or alternatively through microscopic heterogeneity – with small regions with low viscosity [101].

3.3 Dynamics of the Solvation Shell

There are two main modes of ligand exchange; an *associative* where a solvent/anion enters the first solvation shell and subsequently another solvent/anion exits the shell, and a *dissociative* where a solvent/anion exits the shell, creating a vacancy in the shell which is soon filled (Figure 3.6).

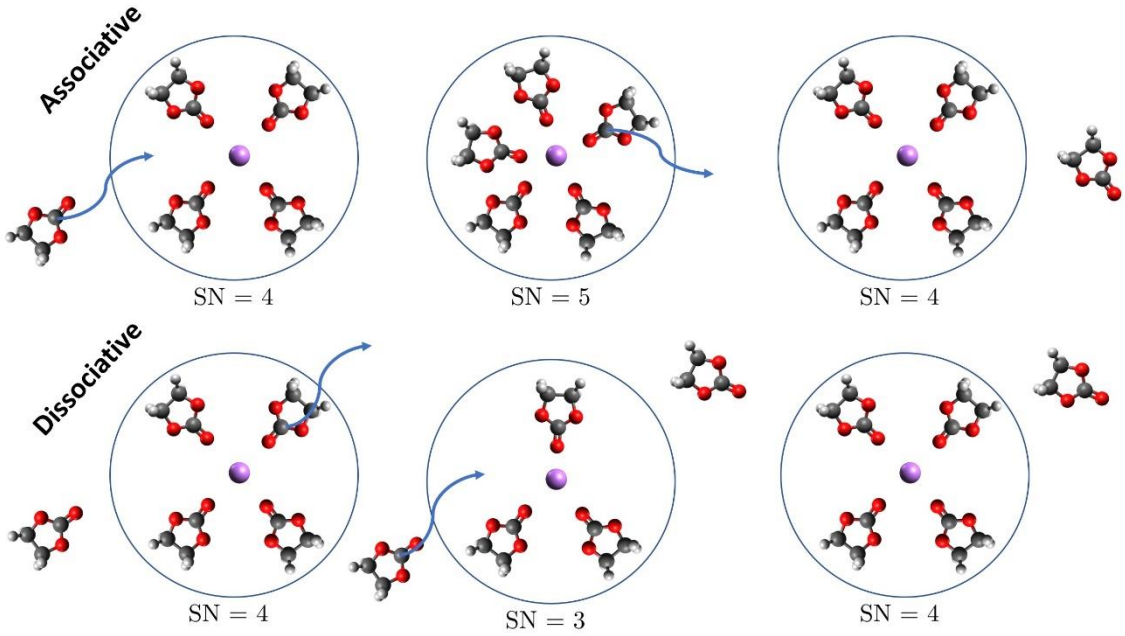

Figure 3.6. Associative and dissociative exchange processes.

There are, however, several dynamic phenomena taking place inside the solvation shell, such as re-orientation of solvents [102], changes in the type of coordination, and possible correlated motion between the solvents/anions in the solvation shell – **Paper I** and **V**.

3.4 Ligand-exchange Rate

The residence time, *i.e.,* the average time τ a solvent/anion remain in a solvation shell, is often studied with MD. A function $H_{l,i}(t)$, where the index l enumerates the ligands and i the cations, is defined

$$H_{l,i}(t) = \begin{cases} 1, & if\ |\boldsymbol{r}_l(t) - \boldsymbol{r}_i(t)| < r_c \\ 0, & otherwise \end{cases},$$

where r_c is a cut-off distance, typically determined from the first minima in an RDF. An autocorrelation function $\xi(t) = \langle H_{l,i}(t) H_{l,i}(0) \rangle$ is then computed. Note that this function is 1 at the start of the run, and then decays to 0 once every solvent has left its original solvation

shell. As ligand exchange is a Poisson process, the function $\xi(t)$ will be proportional to its own time derivative, similar to a radioactive decay process, and thus decays exponentially. A biexponential fit to the autocorrelation function is hence made

$$\xi(t) = Aexp\left(-\frac{t}{\tau}\right)^{\beta} + (1-A)\,exp\left(-\frac{t}{\tau_{short}}\right),$$

where β is a stretch parameter that deviates from unity if several exchange modes at different time scales are present, and τ_{short} is for sub-diffusive processes. Often, the second term in $\xi(t)$ is neglected, and τ and β remain as the only fitting parameters.

Reports on the residence time varies widely, even for the same, or similar systems, from extremely fast dynamical events on the femto-second scale, to the pico-second scale and all the way up to hundreds of nano-seconds [98], [102]–[111].

Here, I suggest a new method of calculating the residence time which relies on computing the average velocity inside the solvation shell.

A ligand exchange is characterized by a solvent/anion moving beyond a critical distance r_c – determined from the minima in an appropriate RDF. Thus, it is inherently a one-dimensional problem. Solvents/anions, however, are extended in space and have their own structures, so there is some ambiguity in how to define when a solvent/anion has exited the solvation shell. Typically, either a specific atom in the solvent/anion, or the entire solvent/anion must move beyond a critical distance. I suggest, however, that to avoid any problems arising due to the structure of the solvent/anion, it is only the centre of mass of the solvent/anion that must move beyond the critical distance.

The radial motion of the solvent/anion centre of mass is completely determined by the forces acting upon the solvent/anion, via Newtons' laws, and the velocities these forces generate. Thus, it should be possible to compute the exchange rate directly from the velocities or forces inside the shell. The ligand-exchange process is, as mentioned, at least approximately a Poisson process and thus stochastic in nature, and some sort of averaging procedure must be used.

If we consider the path Γ_n of a solvent/anion going from inside the shell to outside, the time that solvent spent in the solvation shell is

$$T_n = \int_{\Gamma_n} \frac{dr}{v(r)}.$$

Therefore, the residence time can be computed as an average over all such paths:

$$\tau = \lim_{N\to\infty} \frac{1}{N} \sum_{n=1}^{N} \int_{\Gamma_n} \frac{dr}{v(r)}.$$

If we analyze a single path Γ_n, per definition

$$T_n = \int_{\Gamma_n} \frac{dr}{v(r)} = \frac{d}{\langle v \rangle_n},$$

where $\langle v \rangle_n$ is the average radial velocity along the path Γ_n and d is the change in radial position. All the paths end at r_c, however, the choice of the starting position of the paths appear ambiguous. It could be reasoned that the starting position should simply be where the solvent/anion enters the shell, *i.e.* r_c, as this is the distance that defines the boundary of the solvation shell. But, Γ_n is then a closed path and $\langle v \rangle_n = d = 0$. Instead, we could argue that the solvent/anion is not a part of the first solvation shell until it has equilibrated with it. The starting position of the paths Γ_n could then quite naturally be chosen as the equilibrium distance r_0 inside the shell, *i.e.,* the first peak position in the RDF. Thus, $d = r_c - r_0$ for all paths and

$$\tau = \lim_{N\to\infty} \frac{1}{N} \sum_{n=1}^{N} \int_{\Gamma_n} \frac{dr}{v(r)} = (r_c - r_0) \lim_{N\to\infty} \frac{1}{N} \sum_{n=1}^{N} \frac{1}{\langle v \rangle_n} = (r_c - r_0) \left\langle \frac{1}{\langle v \rangle_n} \right\rangle.$$

Consider the *N* paths. If the radial velocity is sampled at a regular interval, such as in an MD trajectory with a constant time step, we would have *N* sets

$$\begin{aligned} V_1 &= \{v_{11}, v_{21}, \ldots, v_{M_1 1}\} \\ V_2 &= \{v_{12}, v_{22}, \ldots, v_{M_2 2}\} \\ &\vdots \\ V_N &= \{v_{1N}, v_{2N}, \ldots, v_{M_N N}\} \end{aligned}$$

where M_n is the number of samples taken along path Γ_n. For instance, if we ran an MD simulation with a time step Δt, then

$$T_n = M_n \Delta t,$$

where we can make Δt arbitrarily small, *i.e.,* we can go to the continuous limit. Note that if the average velocity $\langle v \rangle_n$ is altered by a factor ζ the time T_n and M_n would change by a factor $1/\zeta$ and we have the general relation

$$\frac{T_n}{T_{n'}} = \frac{\langle v \rangle_{n'}}{\langle v \rangle_n} = \frac{M_n}{M_{n'}}.$$

Using this one can show that

$$\frac{1}{\langle v \rangle} = \left\langle \frac{1}{\langle v \rangle_n} \right\rangle,$$

see **Paper V**. Note that this is not a general property of averages but is true in this case because it is possible to establish an inverse relationship between the average velocity and the number of sample points used to form the average.

Therefore, the residence time can be directly computed from the average velocity inside the shell and the RDF

$$\tau = \lim_{N\to\infty} \frac{1}{N} \sum_{n=1}^{N} \int_{\Gamma_n} \frac{dr}{v(r)} = \frac{r_c - r_0}{\langle v \rangle}.$$

This method relies on few assumptions and is generally applicable to exchange phenomena.

3.5 Conventional Non-aqueous Battery Electrolytes

3.5.1 Solvents

ACN has been a popular solvent due to its combination of being a cheap solvent with a high dielectric constant and low viscosity, yielding high ionic conductivities. ACN based electrolytes, however, yields cells with overall poor electrochemical performance, often due to its narrow ESW, limiting its commercial attractiveness in battery applications, but is a common solvent in commercial supercapacitors outside of China and Japan [19], [87].

Several cyclic carbonates have been used as solvents in battery electrolytes (Figure 3.7). PC has a high dielectric constant, allowing a high degree of salt dissociation, and large liquidus range, and was used extensively in early research on LIBs. However, it was soon discovered that at conventional salt concentrations PC co-intercalates with Li^+ causing exfoliation and degradation of the graphite electrode [112]–[117]. EC has a large dielectric constant and decomposes to form a stable SEI during the first few cycles. Moreover, EC shows no signs of exfoliating the graphite electrode. But EC is liquid first above 36°C and is hence often paired with other solvents in order for the electrolyte to be liquid at room temperature. Linear carbonates (Figure 3.7 generally have a low boiling point and low viscosity, while having a low dielectric constant and are prone to oxidation. The linear carbonates, such as dimethyl carbonate (DMC), diethyl carbonate (DEC) and ethylmethyl carbonate (EMC), are used as co-solvents with EC, which yields an electrolyte liquid at room temperature. Moreover, the ionic conductivity is improved by the addition of a linear carbonate, while EC seems to suppress the oxidative instability of the linear carbonates [117].

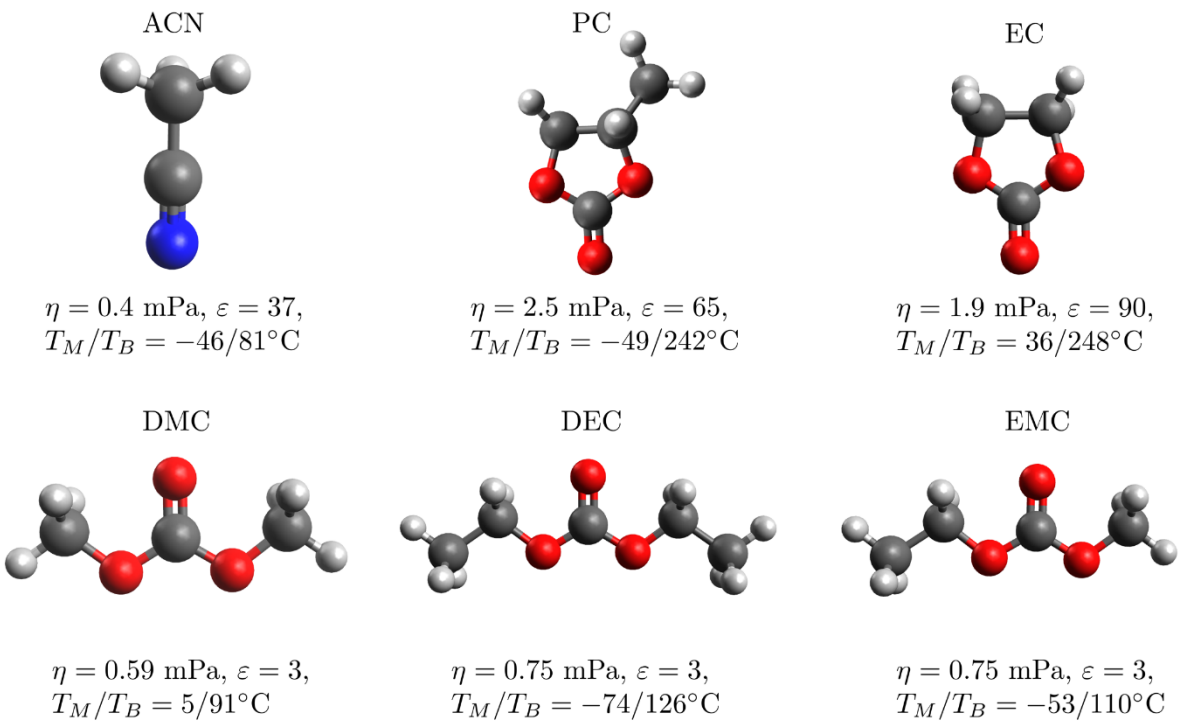

Figure 3.7. Structure of some common solvents and their respective viscosity, dielectric constant, melting and boiling points.

3.5.2 Anions

In order to facilitate adequate ionic conductivity, the salt needs to be able to dissolve and dissociate in the solvent/solvents. Furthermore, the anions need to be chemically stable with respect to the battery components the electrolyte is in contact with. Thus, weakly coordinating anions are often studied for battery electrolytes (Figure 3.8).

Salts with the perchlorate (ClO_4^-) anion show moderate solubility, often yields electrolytes with a relatively high ionic conductivity and SEIs formed with ClO_4^- present in the electrolyte have low impedance. It is often used in lab environments, however, due to being a strong oxidant it is prone to hazardous reactions with organic species, causing explosions at high currents or temperature, thus ruling out its use in commercial cells [117]–[119]. Salts with tetrafluoroborate (BF_4^-) anion are in this company of compounds often relatively difficult to dissociate, but the anion shows high mobility, often leading to a moderate ionic conductivity [117]. Moreover, BF_4^- is a lot safer than ClO_4^-. Electrolytes with hexafluorophosphate (PF_6^-) shows a moderate dissociation constant, and a moderate mobility, and has good oxidative stability. PF_6^-, however, is sensitive to moisture, easily forming HF. Moreover, PF_6^- promotes the formation of a protective film on Al current collectors, protecting them from corrosion

[117]. Finally, bis(trifluoromethanesulfonyl)imide (TFSI) is a weakly coordinating anion popular in research environments, however, it has a strong tendency to corrode Al current collectors [120].

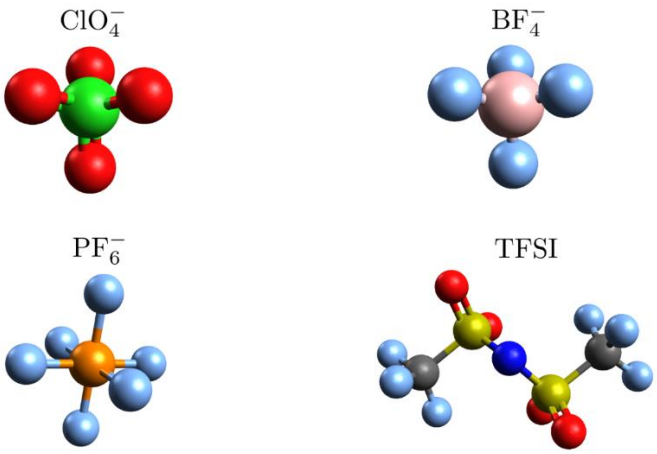

Figure 3.8. The structure of some common anions.

3.5.3 Lithium-ion and Sodium-ion Battery Electrolytes

The conventional LIB and SIB electrolytes use lithium/sodium hexafluorophosphate ($Li/NaPF_6$) as the salt. The rationale being that PF_6^-, while not being outstanding, strikes a good balance between all the properties important for battery electrolytes. The salt concentration is picked to maximise the ionic conductivity, which occurs at *ca.* 1 M in LIB electrolytes. In LIBs the standard LP30 electrolyte is a mixture of EC and DMC in equal volumes. As SIBs have not yet been fully commercialised, no clear standard solvent has emerged, however, the electrolytes investigated for SIBs are similar to the ones found in LIBs [25].

3.6 Highly Concentrated Electrolytes

HCEs for batteries have been an active research subject in recent years [28]–[30]. They display several beneficial properties which, often, derive from the local electrolyte structure (Table 3.1).

Table 3.1. Properties of HCEs.

Advantages/Disadvantages	Origin	References
High rate capability	Less resistive SEI, faster desolvation, high amount of charge carriers	[121]–[123]
Improved energy density	Suppressed Al dissolution, improved electrolyte oxidative stability	[124]–[131]
Improved cycling stability	Anion derived SEI	[132]
Improved safety	Lower vapor pressure, anion derived SEI, higher boiling point, low amount of free solvents	[29], [132], [133]
Increased transport number t_+	New transport mechanism	[94], [95], [99], [100], [105], [106]
High viscosity	Low solvent to salt ratio	[29]
High cost	Expensive salt	[29]

HCEs are dominated by strong ion-ion interactions, and ion-pairs and aggregates are common. There is no fundamental theory for transport in these electrolytes. The strong ionic nature of these electrolytes increases the difficulty of modelling them with MD; the high concentration of charged species polarises the species. Classical force-fields have proven inadequate in accurately modelling HCEs, and instead polarizable force-fields, or AIMD has to be used [134]. These methods, however, carry much higher computational costs – both in terms of memory and CPU hours – limiting the size and time of the simulations.
But, most of the features of the HCEs arise from local electrolyte phenomena, and these are typically only accessible indirectly by experiments. Computer modelling on the other hand has direct access to the local structure, enabling insight into the mechanisms at play, especially the ion transport. Several experimental observations, however, has been made, such as a general increase in viscosity as a function of salt concentration and a decoupling of the molar conductivity from the viscosity, possibly caused by an increase in transport number; 0.2 – 0.4 in conventional electrolytes and >0.7 for HCEs [29].

4. Theory and Computational Methods

Classical molecular mechanics relies on classical force fields that define pair-wise potentials between all atomic types, and represent chemical bonds by classical springs. These methods are computationally inexpensive, but often inaccurate, and are hence often reserved for large macromolecules where more accurate methods are simply to computationally expensive [135]. Moreover, the methods generally do not consider chemical reactions. Similarly, classical MD uses classical force fields and can simulate large systems, but special care has to be taken for electrolyte systems as to not compromise accuracy too much [134]. Instead, we turn to quantum chemical methods that explicitly treat the electronic structure. These methods are considered accurate, but are considerably more computationally expensive [136].

4.1 Quantum Chemistry and the Schrödinger Equation

The fundamental equation governing all non-relativistic systems is the Schrödinger equation [137], succinctly expressed as

$$H\Psi(r,t) = i\hbar\frac{\partial\Psi(r,t)}{\partial t},$$

where $\Psi(r,t)$ is the wavefunction, $r = (x,y,z,\sigma)$, σ is the spin of the particle, and H is the Hamiltonian of the system. Often, we only consider the time-independent Schrödinger equation $H\Psi(r) = E\Psi(r)$, where E is the energy of the system.

However, no analytical solutions exist for any atomic system with more than a single electron, as famously noted by Dirac "*The underlying physical laws necessary for the mathematical theory of a large part of physics and the whole of chemistry are thus completely known, and the difficulty is only that the exact application of these laws leads to equations much too complicated to be soluble.*" and hence large parts of this chapter will focus on how the wavefunction can be approximated and the Hamiltonian simplified [138].

The first of these simplifications is the Born-Oppenheimer approximation. The proton has three orders of magnitude more inertia than the electron. Hence, nuclei move more sluggishly than electrons. Therefore, the electrons will have much higher average velocities and thus equilibrate quickly with respect to any changes in the position of the nuclei and we can hence consider the electrons as moving in a static distribution of nuclei. The motion of the nuclei and electrons thus decouples, and the total wavefunction can be decomposed into an electronic wavefunction $\psi(r_1,\dots,r_N;R_1,\dots,R_K)$, that depends on the coordinates of the

nuclei, and the wavefunction of the nuclei $\xi(R_1, \dots, R_K)$. This approximation is assumed in all of the subsequent methods discussed.

4.1.1 Representing the Wavefunction

Feynman famously argued that the exponential increase, with the size of the system, of the amount of memory required to store an exact representation of the wavefunction of the system is unreasonable. After all, the information of a system is contained within the volume of the actual system, hence it should be possible, in principle, to store an accurate representation of a system in a unit that scales linearly with the volume of the system [139]. As this is impossible on a classical computer [140], the first practical issue is to represent the wavefunction. Often the single-electron wavefunction, or molecular orbital, Φ_n is written in a basis set of functions, atomic orbitals, φ_μ centred on the nuclei. The atomic orbitals can in turn be written as linear combinations of, usually, gaussian functions

$$\varphi_\mu = \sum_i d_{\mu,i}\, g_i(\zeta, r)$$

where

$$g_i(\zeta, r) = C x^{n_i} y^{m_i} z^{l_i} \mathrm{e}^{-\zeta_i r^2},$$

where C is a normalization constant, n_i, m_i and l_i determines the shape of the function (s, p, d, and so on, type orbital), and ζ_i determines the width of the function. Once a basis set is selected, *i.e.* a set of φ_μ, the molecular orbital can be written as

$$\Phi_n = \sum_\mu c_{n,\mu}\, \varphi_\mu.$$

The complete wavefunction $\psi(r_1, \dots, r_N; R_1, \dots, R_K)$ is then written as a superposition of the single-electron molecular orbitals [135]. In practice, a guess of the molecular orbitals is made, *i.e.,* a guess for all the coefficients, and the energy $\epsilon = \int \psi^* \mathrm{H} \psi \mathrm{dV}$ is computed. The variational principle states that

$$\mathrm{E}_0 \leq \epsilon,$$

where E_0 is the true ground state energy [137]. Thus, a numerical solution to the Schrödinger equation can be found through progressively, and systematically, making better and better guesses for the wavefunction, yielding lower and lower energies, until a convergence criterion is met.

The wavefunction can subsequently be used to define the electron density

$$n(r) = \sum_{n=1}^{N} |\Phi_n(r)|^2,$$

and

$$\int n(r)\, d\tau = N.$$

4.1.2 Hartree-Fock Theory

One approach to numerically solve the Schrödinger equation is due to Hartree and Fock [141]. As electrons are fermions, their wavefunctions must be anti-symmetric. Thus, by writing the total wavefunction as a single determinant of molecular orbitals the Pauli principle is enforced. Note that this introduces correlation into the system and an additional interaction term for electrons with parallel spin [142].

Finally, to simplify electron-electron interactions, electrons are assumed to only interact with one-another through a mean field [135], [142]. These approximations and assumptions lead to the Fock equation

$$F\Phi_n = \varepsilon_n \Phi_n$$

where ε_n is the energy of the molecular orbital Φ_n, and F is the Fock operator:

$$F = T + V_{ion-e} + J - K,$$

where T is the kinetic energy operator, V_{ion-e} the nuclear-electron attraction operator, and J and K are the Coulomb and exchange operators, respectively:

$$J\Phi_n(r) = \left(\sum_{m=1}^{occupied} \int \Phi_m^*(r') \frac{1}{r - r'} \Phi_m(r') d\boldsymbol{r'} \right) \Phi_n(r),$$

$$K\Phi_n(r) = \left(\sum_{m=1}^{occupied} \int \Phi_m^*(r') \frac{1}{r - r'} \Phi_n(r')\, d\boldsymbol{r'} \right) \Phi_m(r).$$

Note that $J\Phi_n(r)$ is the electron *n* interaction with the mean field created by all other electrons, including itself, while $K\Phi_n(r)$ is called the exchange term and is a non-local interaction as the operation on $\Phi_n(r)$, depends on $\Phi_n(r)$ at all positions. The self-interaction term arising from the Coulomb operator is exactly cancelled by a term in the exchange operator. Moreover, the exchange operator is only non-zero for electrons with parallel spin [142].

Furthermore, the Roothaan-Hall matrix equation can be formed,

$$\boldsymbol{FC = \varepsilon SC}$$

where **C** is the matrix of molecular orbital coefficients $c_{i,\mu}$, $\boldsymbol{\varepsilon}$ is a diagonal matrix containing the molecular orbital energies ε_i, and **S** is an overlap matrix $S_{\mu\nu} = \int \varphi_\mu \varphi_\nu d\,\tau$.

The Fock operator, along with the overlap matrix in the Roothaan-Hall matrix equation depends directly on the molecular orbitals Φ_i. Thus, to solve the equations an initial guess for the molecular orbitals is made, the matrices are then diagonalized, yielding new eigenstates Φ_i' and energies ε_i'. These new orbitals can then be used to yet again form the Fock operator, and this process is iterated until some convergence criteria is met. This is the self-consistent field (SCF) approach (Figure 4.1) [135], [142], which all the subsequent methods rely on.

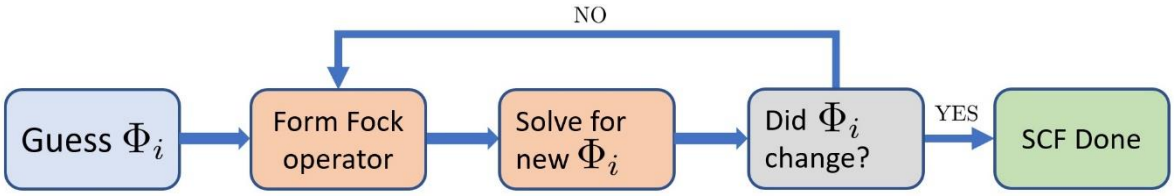

Figure 4.1. The SCF loop.

4.1.3 Semi-empirical Methods

Using empirical data, or data from high level *ab initio* methods, the computational cost of solving the Roothaan-Hall matrix equation can be substantially reduced. A large family of semi-empirical methods assume the atomic orbitals are orthogonal, in what is called the neglect of diatomic differential overlap (NDDO), and hence **S** is simply the identity operator. The parametrized methods, a subset of the NDDO methods, are optimized to give accurate energies, and use empirical data to partially determine off-diagonal elements in the Fock matrix [143], [144] – PM7 is used in **Paper I** [143]. The semi-empirical methods are computationally inexpensive – meaning that large systems, consisting of several solvation shells, can be readily simulated on a modern day laptop.

4.2 Density Functional Theory

DFT is used extensively in **Paper III-V**, is used frequently in the field **Paper II,** and is used in the majority of electronic structure calculations [142]. DFT utilizes the electron density, rather than the wavefunction of the system, thus the number of coordinates needed to describe the system is reduced from $3(N + K) - 6$ to simply 3. DFT is considered accurate [136], however, the computational cost of DFT scales exponentially with the number of

atoms in the system – the exact scaling depends on the functional and basis used – and hence the systems simulated are seldomly larger than a single solvation shell.
DFT is made possible by two theorems by Hohenberg and Kohn that shows that there is a unique map between the electron density and the ground state properties of the system [145]:

Theorem 1*: The ground state electron density uniquely determines the external potential of the system, and thus the whole Hamiltonian.*
Theorem 2*: A universal functional, valid for any external potential, can be defined in terms of only the electron density.*

Furthermore, the energy of the ground state of the system can be calculated from the electron density:

$$E_0 = T[n(r)] + \int_{R^3} V_{nuclei}(r)n(r)\,dr + \frac{1}{2}\frac{1}{4\pi\varepsilon_0}\int_{R^3}\frac{n(r)n(r')}{|r-r'|}drdr' + E_{xc}[n(r)]$$

where $T[n(r)]$ is the kinetic energy functional of a non-interacting electron gas, V_{nuclei} is the potential generated from the nuclei, and $E_{xc}[n(r)]$ is a functional which containing the remaining energy [142].
To make use of the Hohenberg and Kohn theorems the electron density must first be determined. This is done with the Kohn-Sham equation:

$$\left(-\frac{\hbar^2}{2m_e}\nabla^2 + V_{eff}(r)\right)\psi_i(r) = \varepsilon_i\psi_i(r),$$

where

$$V_{eff}(r) = V_{nuclei}(r) + \frac{1}{2}\frac{1}{4\pi\varepsilon_0}\int_{R^3}\frac{n(r')}{|r-r'|}dr' + \frac{\delta E_{xc}[n(r)]}{\delta n(r)}. \quad \textbf{(1)}$$

The electron density is then found by a SCF approach [146].
The last term in the effective potential (equation 1) is also called the exchange-correlation potential:

$$\frac{\delta E_{xc}[n(r)]}{\delta n(r)} = V_{xc}[n(r)].$$

The various functionals of DFT approximates $V_{xc}[n(r)]$, generally by expanding the exchange-correlation potential in terms of the electron density:

$$V_{xc}[n(r)] = V_{xc}[n(r), \nabla n(r), \nabla^2 n(r), \dots].$$

The functionals are often organized in a ladder, from simple and computationally inexpensive to accurate and computationally expensive [147]. In **Paper III** and **IV** the Minnesota

functional M06-2X is used [148], which has been shown to give accurate results for battery electrolyte systems [136], [149]. The generalized gradient approximation PBE functional by Perdew, Burke and Ernzerhof was used in **Paper IV** [150].

4.3 *Ab initio* Molecular Dynamics

The Hellmann-Feynman theorem shows that the force on nuclei k is

$$F = -\frac{\partial E}{\partial R_k} = -\left\langle \Psi \left| \frac{\partial H}{\partial R_k} \right| \Psi \right\rangle = \mathrm{Z_k} \left(\int \mathrm{n(r)} \ \frac{\mathrm{r} - \mathrm{R_k}}{|\mathrm{r} - \mathrm{R_k}|^3} \mathrm{dr} \ - \sum_{\mathrm{l} \neq \mathrm{k}}^{\mathrm{K}} \frac{\mathrm{Z_l}(\mathrm{R_l} - \mathrm{R_k})}{|\mathrm{R_l} - \mathrm{R_k}|^3} \right),$$

i.e., the force on nuclei k is simply determined by the electron density $\mathrm{n}(\mathbf{r})$ and the coulomb interaction between the nuclei [151]. Therefore, once the electron density is found the forces on the nuclei can be computed. Once the forces are known, the acceleration on the nuclei can be calculated through Newtons' second law. Thus, in principle AIMD is possible by computing the electron density from an initial configuration of nuclei, from which the forces, and accelerations, on each nucleus is calculated. Then a small time step is taken where each nuclei is displaced according to its acceleration and initial velocity, and the procedure is repeated again. Computing the electron density, however, is computationally expensive, and doing so at each time step becomes practically unfeasible for any moderate system size [142]. This problem was tackled by Car and Parrinello, who combined the quantum mechanical approach with the classical approaches to MD [152]. Writing the total energy as a functional of the electronic wavefunctions and the nuclear positions,

$$E_{tot} = E_{tot}[\{\psi_i\}, \{R_j\}],$$

and endowing the electrons with kinetic energy such that a time dependence can be assigned to the electronic wavefunctions, allowed Car and Parrinello to construct a classical Lagrangian

$$L(\{\psi_i\}, \{R_j\}) = \frac{\mu}{2} \sum_{i=1}^{N} |\dot{\psi}_l|^2 + \frac{1}{2} \sum_{j=1}^{K} M_j \, \dot{R}_j^{\,2} + E_{tot}(\{\psi_i\}, \{R_j\}) + \sum_{kl} \Lambda_{kl} \langle \psi_l | \psi_k \rangle.$$

The parameter μ is a fictitious electron mass that must be chosen small enough to allow the electronic wavefunctions to adapt to the changing position of the nuclei, but large enough to allow for time steps of practical significance. The Lagrange multipliers Λ_{kl} are introduced in order to fulfil any external constraints, such as the orthonormality condition on the electronic wavefunctions. Using this Lagrangian, the Euler-Lagrange equation of motions are

$$\begin{cases} \mu\ddot{\psi}_i = -\dfrac{\partial E_{tot}}{\partial \psi_i} + 2\sum_j \Lambda_{ij}\psi_j \\ M_j\ddot{R}_j = -\dfrac{\partial E_{tot}}{\partial R_j} + \sum_{kl} \Lambda_{kl}\dfrac{\partial \langle \psi_k | \psi_l \rangle}{\partial R_j} \end{cases}$$

which are the equations solved in CPMD [142] – used in **Paper V**.

AIMD requires considerably more computational resources than classical MD – currently restricting the simulations to $10^2 - 10^3$ atoms and simulation times of a few tens of pico-seconds, while classical MD can handle $10^4 - 10^5$ atoms and simulate the nano-second scale. Great care, however, has to be taken when using classical MD on highly ionic systems, as the accuracy can often be poor, especially for transport properties [134].

4.4 Geometry Optimizing Molecular Systems and Computing Spectra

The equilibrium structure of a molecule, or a system of molecules, is the positions of the nuclei such that no net forces act on them. To find the equilibrium structure the geometry of the system is optimized by utilizing gradient descent, with respect to the nuclear coordinates R_k, of the total energy in order to locate a stationary point in the potential energy surface (PES). Once a set of nuclear coordinates have been found such that

$$F = \frac{\partial E}{\partial R_k} = 0,$$

a stationary state has been located. The stationary state, however, does not necessarily correspond to a minimum in the PES, *i.e.,* a stable equilibrium structure, but can be an unstable equilibrium, a saddle point in the PES, which can correspond to a transition state. To ascertain the nature of the stationary state a frequency calculation can be made. If a Taylor expansion of the potential energy is carried out around the stationary point the potential can be written as

$$U = \frac{1}{2}\frac{\partial^2 U}{\partial R_k\, \partial R_l} R_k R_l = \frac{1}{2} U_{k,l} R_k R_l,$$

where $U_{k,l} = U$ is the Hessian. The kinetic energy can be expressed as

$$T = \frac{1}{2} m_{k,l} \dot{R}_k \dot{R}_l,$$

where $m_{k,l} = m$ is a diagonal matrix containing the masses of the nuclei. The structure of the potential indicates a harmonic oscillator behaviour and

$$R_k = C a_k e^{-i\omega t}.$$

Thus, the equation of motion becomes

$$U - \omega^2 m = 0,$$

and the frequencies can be determined from taking the determinant of this equation [153]. If all the frequencies ω are positive the stationary state is situated in a minimum in the PES and corresponds to a stable equilibrium structure. If, however, a frequency is imaginary, the state corresponds to a transition state, connecting two minima in the PES, one representing a product, one representing a reactant. If more than two frequencies are imaginary, the stationary state is located on a higher order saddle point [135] [154], [155].
To compute the IR intensities, or Raman activities, associated with the frequencies higher order derivatives needs to be computed. The derivative $\partial^2 E / \partial R_k \partial F$, where F is an external electric field, is proportional to the change in dipole moment during the vibration and thus yields IR intensities, while $\partial^3 E / \partial R_k \partial F^2$ is proportional to the change in polarizability during vibration, hence the derivative gives the Raman activities – these were used in **Paper IV** to scale the experimentally observed IR and Raman data.

The geometry calculations are carried out at 0 K. However, the normal modes revealed by a frequency calculation, along with the electronic energy and the moment of inertia of the system, allows for the construction of the partition function. Thermodynamic properties, at non-zero temperature, can then be directly calculated from the partition function. These calculations, however, assume an ideal gas behaviour, and that the system is in the electronic ground state, and hence the accuracy of these calculations is uncertain [156].
Generally, an electronic structure computation starts by defining the coordinates of all the nuclei, along with the total charge and spin multiplicity of the system. This is proceeded by a geometry optimization, where the electronic structure is computed for each new set of nuclear coordinates, be it by DFT, semi-empirical or some other quantum chemical methods. Once the geometry has converged on a stationary state a frequency calculation is made to affirm that the structure is a stable, *i.e.*, represents a minimum in the PES, and yields the free energies of the system – this general methodology was used in **Paper I**, **III** and **IV**.

5. Results

5.1 Solvation Shell Structure

Due to being great solvents, with high dielectric constants, wide liquid range and low viscosity, PC and ACN are of interest for HCEs. Moreover, they practically allow for reversible Li^+ intercalation in graphite at high salt concentrations [121], [157] – which is thought to be related to the local electrolyte structure.

The first solvation shell content and structure of Li/$NaPF_6$ in PC or ACN, as a function of salt concentration was extensively studied using PM7 geometry optimized structures (**Paper I**), and by CPMD (**Paper V**). Moreover, the CN and SN of $LiPF_6$ in PC electrolytes were studied comprehensively using IR/Raman, DFT and CPMD (**Paper IV**).

The RDFs (**Paper I**, **IV**, and **V**) shows how the content of the solvation shell changes with salt concentration; increasing the salt concentration leads to less nitrogen/oxygen in the first solvation shell, and more fluorine. Even if PM7 and CPMD give qualitatively the same overall results, several differences can be seen. The position of the first peak is in general further out (by 0.1 – 0.3 Å) in the PM7 study, and hence the PM7 predicts larger shell sizes. In view of the Stokes-Einstein relation, larger shells typically indicate a lower diffusion coefficient and ionic conductivity. The main difference, however, seems to be associated with the anion. CPMD places the fluorine and nitrogen/oxygen peaks at approximately the same distance from the central cation, but PM7 predicts that fluorine is 0.2 Å closer to Na^+ than oxygen, and Li^+ than nitrogen, but 0.2 Å further out than nitrogen is to Na^+. The Na^+ shell is larger than the Li^+ shell, indicating that interactions between Na^+ and the solvents/anions are weaker compared with Li^+, hence it should be easier to desolvate Na^+ *vs.* Li^+, which should lead to lower impedance and faster rate capabilities for SIBs – which has been observed [158].

Both PM7 and CPMD shows a CN of *ca.* 6 for Na^+, consistent with other studies [159]–[161], while CPMD predicts a CN of *ca.* 4 for Li^+ and PM7 4.5 – 5. Although results differ somewhat between studies, the general consensus is that the total CN of Li^+ is 4 – **Paper IV**. The difference in CN between Li^+ and Na^+ has several implications for battery electrolytes, and HCEs in particular. As Na^+ has a greater CN than Li^+, at the same solvent to salt ratio there must either be more anions and/or solvents in the Na^+ solvation shell, compared with the Li^+ first solvation shell. Thus, there are more CIPs/aggregates and/or less free solvents in a SIB electrolyte, compared with a LIB electrolyte at the same solvent to salt ratio. Thus, some HCE properties should emerge at lower salt concentrations in SIB electrolytes.

Comparing the results for the partial CNs from **Paper I** and **V**, the same trends are seen – The amount of fluorine in the first solvation shell increases, while the amount of oxygen decreases with increased salt concentration, and both methods show that Na^+ has a higher variance in the CN than Li^+ – but there are some major quantitative differences (Table 5.1). PM7 consistently predicts a much higher fluorine content in the first solvation shell than CPMD, and a considerably higher CN variance (Table 5.1), but both methods show that the variance increases with concentration.

Table 5.1 Li^+/Na^+ CNs in PC based electrolytes.

Salt	**Concentration**	$\boldsymbol{CN_O}$		$\boldsymbol{CN_F}$		$\boldsymbol{Var(CN_{tot})}$	
		PM7	**CPMD**	**PM7**	**CPMD**	**PM7**	**CPMD**
$LiPF_6$	20:1 (dilute)	4.3±0.3	3.6±0.3	0.9±0.2	0.2±0.2	1.5	0.4
	10:1 (conc.)	3.4±0.2	3.3±0.4	0.9±0.2	0.4±0.2	2.3	0.5
	5:1 (highly conc.)	2.9±0.2	2.3±0.3	1.8±0.2	1.3±0.4	2.2	0.5
$NaPF_6$	20:1 (dilute)	4.8±0.3	5.6±0.6	1.5±0.4	0.1±0.2	2.9	1.6
	10:1 (conc.)	4.0±0.2	5.0±0.6	1.7±0.2	1.0±0.5	3.5	1.5
	5:1 (highly conc.)	2.7±0.2	3.6±0.4	3.6±0.4	3.4±0.5	5.4	1.6

Both methods, however, considerably overestimate the number of fluorine/anions in the solvation shell compared with the experimentally determined values (**Paper IV**). The IR/Raman measurements determine SN_{anion} – the number of anions in the cations first solvation shell – by measuring the concentration of free anions $[PF_6^-]_{free}$. The average number of anions in the solvation shell can thus be computed

$$SN_{anion} = \frac{[LiPF_6] - [PF_6^-]_{free}}{[LiPF_6]},$$

where $[LiPF_6]$ is the salt concentration. The measurements indicate that there is on average 0.3 – 0.4 anions in the solvation shell at the highest possible concentration (3.2 M, roughly 3 solvents per salt). This method, however, fails to account for anions being shared between cations, such as in aggregates, which might account for some of the discrepancy seen between the computational and experimental results.

The computed and measured average number of solvents in the solvation shell SN_{Li-PC} largely agree (**Paper IV** and **V**), with an average of 4 PC molecules in the solvation shell at dilute concentrations. Moreover, in **Paper IV**, we found that the SN_{Li-PC} changes very slowly with salt concentration until it enters a highly concentrated regime – and it starts to drop linearly. This occurs at the same salt concentration as the concentration of free PC drops below the salt concentration, and there are more free anions than solvent, which also coincides with a suppression of the PC induced graphite exfoliation, and the cell can be reversibly cycled (Figure 5.1).

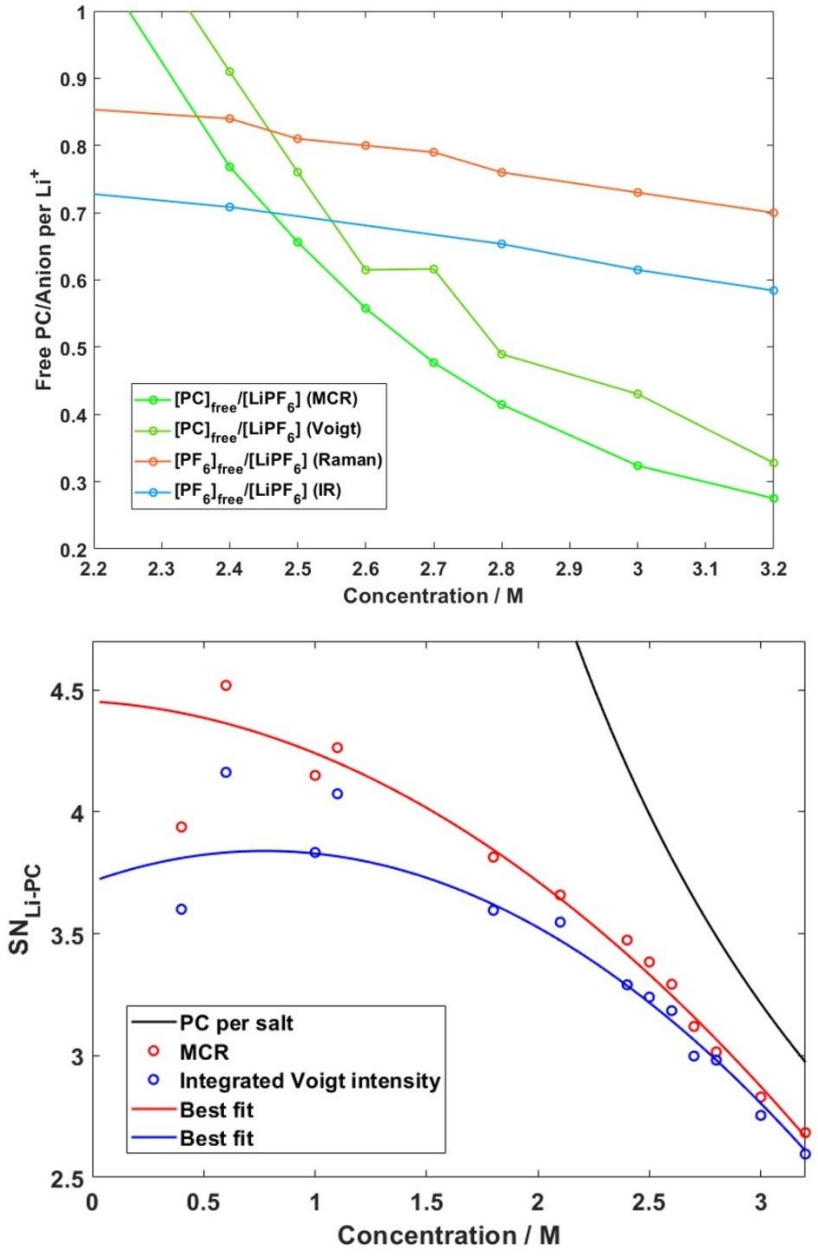

Figure 5.1. (Left) Free solvents and free anions as a function of concentration. (Right) Average number of PC in the Li^+ solvation shell as a function of concentration.

5.1.1 Angle Distributions

PM7 and CPMD both suggest tetrahedral coordination for Li^+ and octahedral for Na^+ (**Paper I** and **V**). Moreover, in a PC based electrolyte the cation can coordinate to both the carbonyl oxygen and one of the etheric ring oxygen atoms. In such bidentate coordination the angle between the two oxygen atoms and the cation are considerably much smaller (*ca.* $50°$) than between two oxygens from two different PC molecules in the solvation shell and the cation. Comparing the angle distributions for PC, **Paper I** and **V**, it is clear that both PM7 and CPMD predicts bidentate coordination. Thus, it seems that PM7 predicts the same general trends in content and structure of the solvation shell, compared with CPMD, even though it was optimized for energy calculations. But, the quantitative differences between the methods are clear, and it seems that the major differences between PM7 and CPMD are related to their treatment of the anion.

5.1.2 Solvent-ion and Ion-ion interactions

Several studies have investigated the differences in ion-ion and ion-solvent interactions between Li^+ and Na^+ [149], [162]–[165], and a meta-study showed that quite broadly, regardless of the exact ion-ion or ion-solvent interaction, the interaction energies are lowered by *ca.* 20% upon using Na^+ instead of Li^+ as the cation – **Paper II**. Generally, this is taken as an indication that desolvation occurs more readily in a SIB electrolyte, and lower interfacial impedance and faster kinetics ensues.

Interaction energies can also be used to predict energetically stable solvation shells, again showing that Li^+ prefers a solvation shell consisting of four solvent molecules – **Paper IV**. Energy calculations, however, fails to account for concentration dependencies on the solvation shell structure, as these calculations are usually limited to only modelling a single solvation shell.

The solubility of O_2 was studied in **Paper III**, important for the capacity of metal-air batteries. The interaction energy between O_2 and several anions was computed and followed the solubility trends observed in experiments – a strong interaction led to an increase in solubility, while a weak interaction led to a decrease in solubility, with increasing salt concentration.

5.2 Dynamics of the Solvation Shell

5.2.1 Forces and Potentials

The solvation shell is continuously poked and prodded on by its environment, and the forces acting on the solvation shell are stochastic. Looking at the probability distribution of the radial forces on the solvent molecules centre of masses as a function of distance from a cation a clear picture emerges (Figure 5.3) – **Paper V**. The radial forces inside the first solvation shell are centred around a linear feature, while the force distribution in the second solvation shell is centred around a force of zero. Integrating the average radial forces shows that the solvents are locked in a harmonic oscillator well inside the first solvation shell (Figure 5.4).

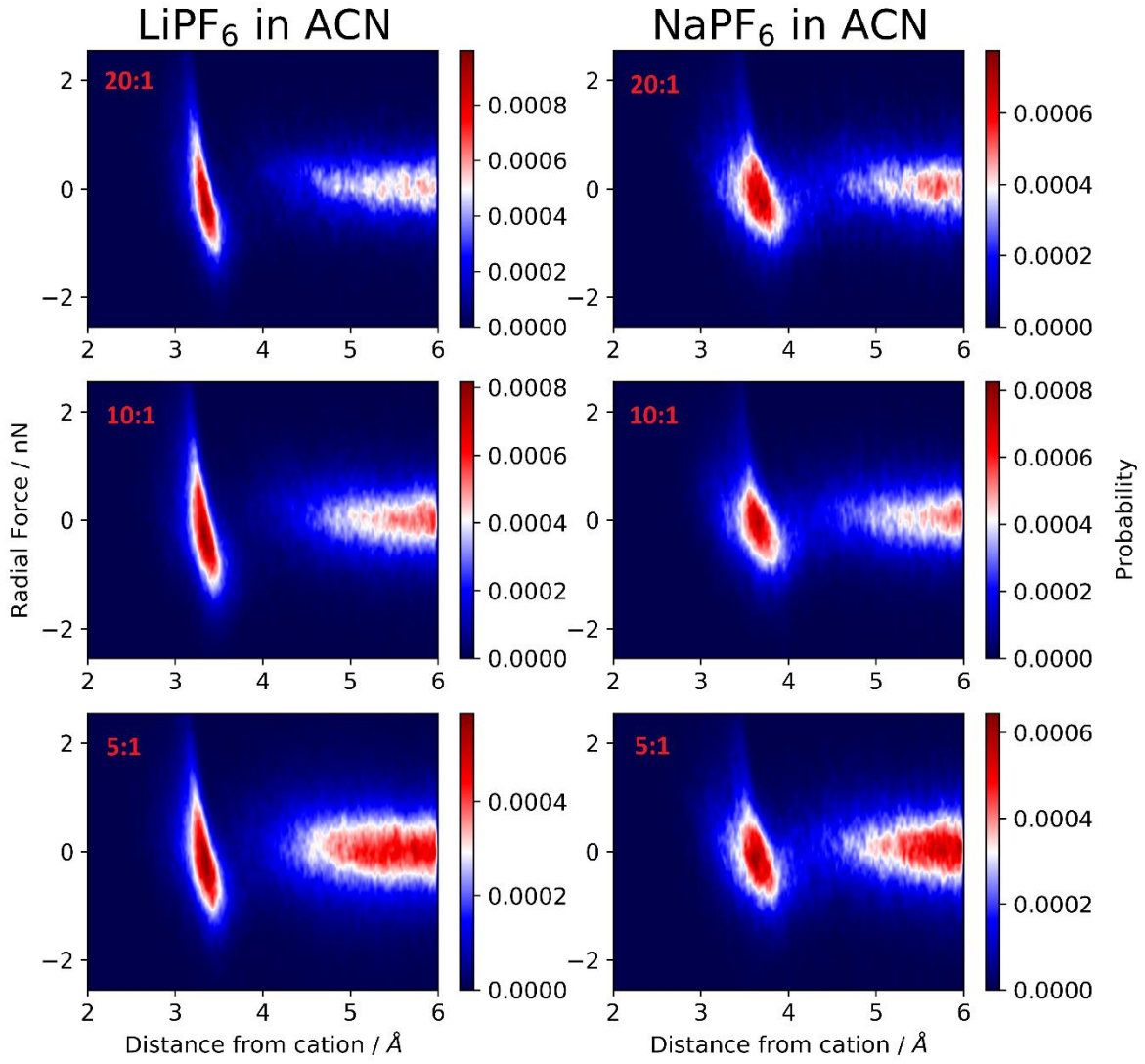

Figure 5.3. Heat map of the probability distribution of the radial forces, on the ACN centre of mass, as a function of ACN centre of mass distance to the cation.

Comparing Na^+ and Li^+, the forces are stronger on the solvents in the Li^+ solvation shell, and the solvents are less confined in the Na^+ solvation shell. Moreover, the energy barrier between the first and second solvation shell are smaller in the Na^+ case. Therefore, ligand exchange should occur more frequently, and desolvation should be easier, in the Na^+ electrolyte, compared with the Li^+, consistent with the results discussed in section 5.1, and with experimental observations.

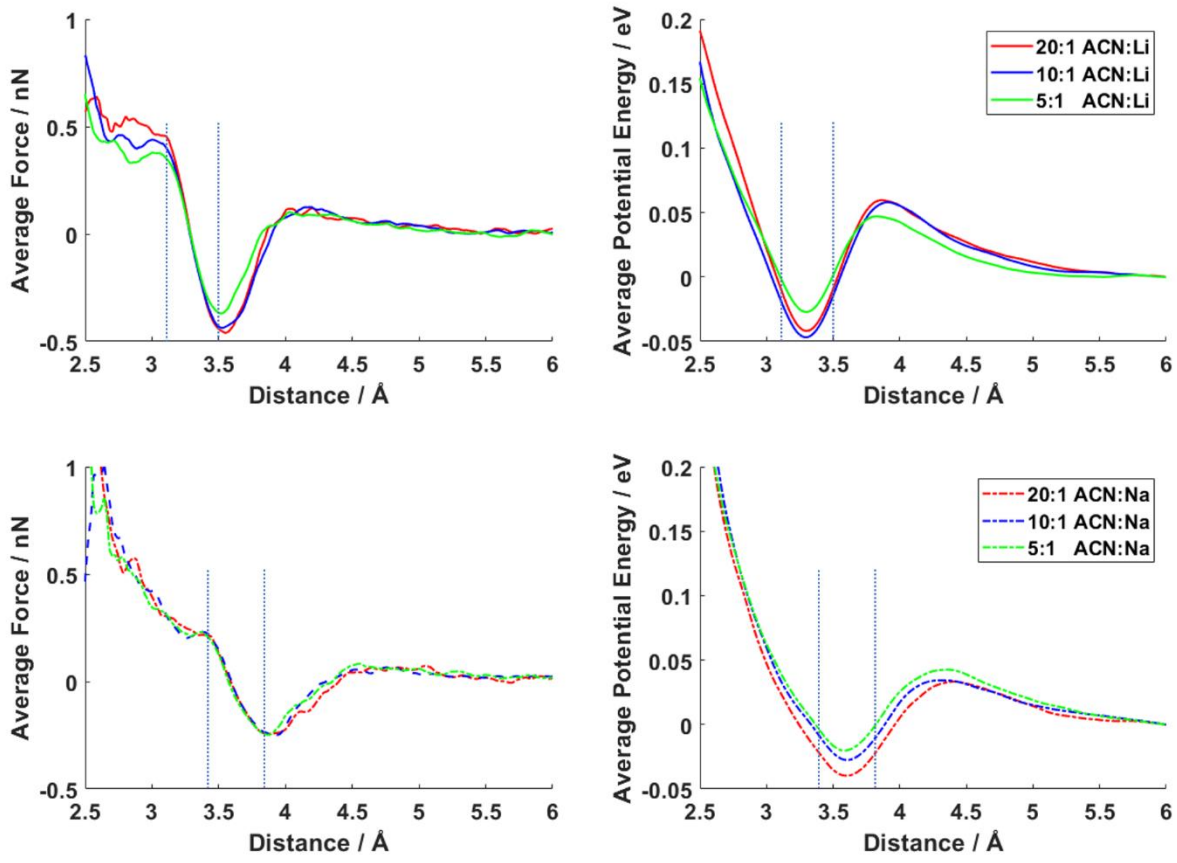

Figure 5.4. Average forces and potentials on solvents in solvation shells.

5.2.2 Velocities

Studying the radial velocities, which are symmetrically distributed around zero – both in the first and second solvation shell – but greater in the Li^+ solvation shells, also consistent with stronger interactions (Figure 5.5). Moreover, as this is the radial velocity, and the data is gathered for all solvents, independent of if they start in the solvation shell or not, the distributions must be centred on zero as there is no net flux in or out of the shell. The width,

however, of the distributions should be determined by the ion-solvent interactions, along with the temperature of the system.

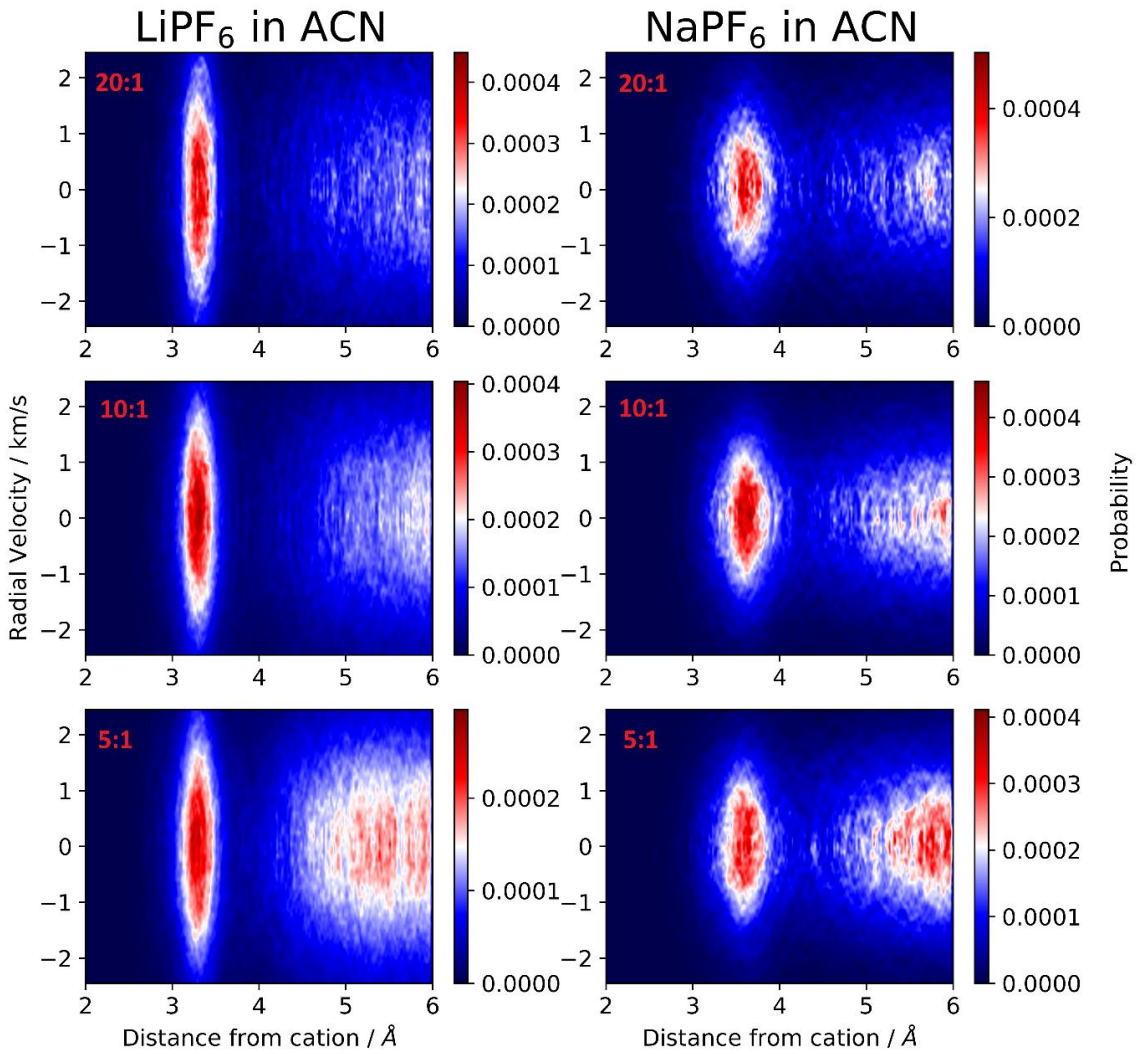

Figure 5.5. Heat map of the probability distribution of the radial velocities, on the ACN centre of mass, as a function of ACN centre of mass distance to the cation.

5.2.3 Ligand-exchange

The force distributions and potential barriers only give indirect information about the exchange-rate and processes. Turning to these processes directly, the CPMD simulations of **Paper V** saw one or several exchange events for the majority of the solvation shells. Both associative and dissociative processes were observed (Figure 5.6), but the former dominated. Moreover, the associative process was often preceded by several failed attempts where the

solvent very briefly entered the shell and subsequently was ejected (orange line, bottom panel, Figure 5.6).

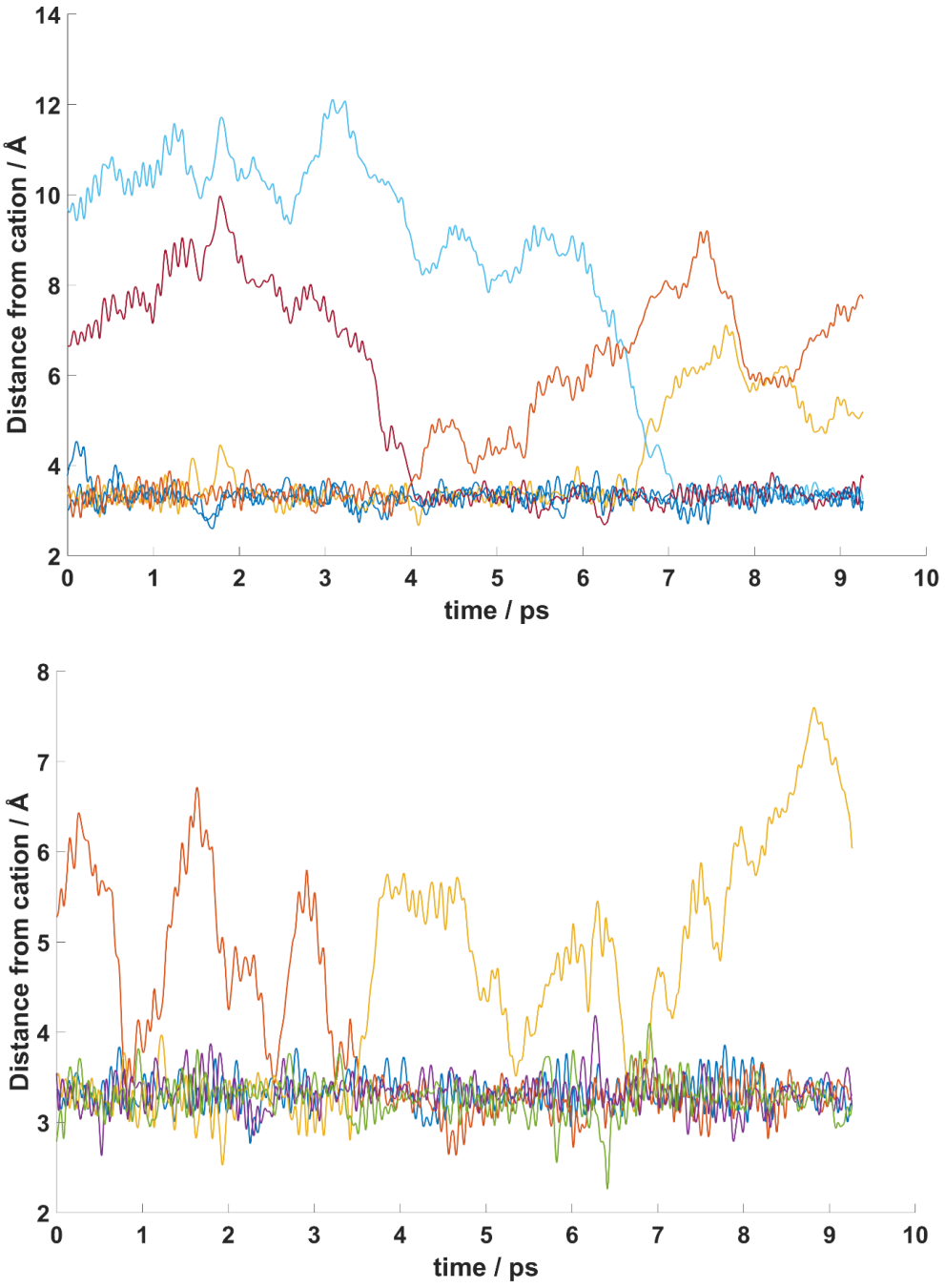

Figure 5.6. The distance between a cation and all solvents that spent any time inside its first solvation shell. (Top) Two dissociative exchanges at 4 and 7 ps. (Bottom) Associative exchange at 3.5 ps.

In **Paper V** the residence time was computed with the new method described in Chapter 3. The residence time generally decreased with the salt concentration and was lower for Na^+ than for Li^+. The residence times (*ca.* 10 – 15 ps in the ACN based electrolytes and *ca.* 1 – 3 ps in the PC based electrolytes) differ somewhat from previous results. For the ACN system, the results are in good agreement with previous studies, having found residence times between 25-100 ps using classical MD [98], [111]. While for $LiPF_6$ in PC the residence time was recently computed to be 1000 – 10000 ps using classical MD [105]. Several other studies have found residence times ranging from the pico-second to nano-second scale [98], [102]–[111]. There are several possible explanations for the discrepancies in the literature – starting with the possibility that different systems can have vastly different residence times. Moreover, the classical force-fields, and the types of AIMD used, differ, which can lead to substantially different results [134]. Moreover, the size and simulation times are vastly different for classical MD and AIMD, and hence the simulations might probe different exchange modes. For instance, in [105] they fit a bi-exponential function to the auto-correlation function, and computes two residence times, τ and τ_{short}. But, τ_{short} is never presented, and a smoothing function was applied to remove events that occur on the τ_{short} scale. Therefore, it is possible that some discrepancies in the literature arises because classical MD studies simply overlook the fast pico-second events, while the AIMD simulations cannot access the processes occurring on the nano-second scale.

6. Summary and Conclusions

In this thesis, several computational methods were employed to study the structure and dynamics of the solvation shell of battery electrolytes. Several of the studies found similar results, and an overall picture emerged of the salt concentrations strong influence on the local electrolyte environment – increasing the anion content in the first solvation shell and decreasing both the concentration of free solvents, and the solvent content of the first solvation shell, as the concentration is increased. The energetically most stable solvation shells, however, only contain solvents. Therefore, increasing the salt concentration ease desolvation which facilitates the observed improvements in kinetics. Moreover, the electrolyte grows more heterogeneous, as measured by the variance of the CNs, with increasing salt concentration, again indicating that the stability of the solvation shells decreases with increasing salt content. The solvent residence time was computed with a new and generally applicable method showing that ligand exchange is more prevalent at high salt concentrations – which relates to both the observed improvements in kinetics, and the altered transport mechanism in HCEs.

Several of the studies compared LIB and SIB electrolytes. It was found that the properties associated with HCE, such as increased CN variance, less energetically stable solvation shells, and shorter residence time, was more pronounced in the SIB electrolytes. Moreover, the CN and SN of Na^+ is higher than for Li^+, thus the electrolyte becomes deprived of free solvents at lower salt to solvent ratios in SIB electrolytes. Taking these observations in conjunction, SIB electrolytes should show a strong onset of some HCE features at lower salt concentrations than LIB electrolytes.

Several comparisons were also made between ACN and PC, showing that PC, just as Na^+ promotes the features associated with a HCE, showing much shorter residence time and a higher disorder, both in terms of dynamical properties such as the force and velocity distributions, but also in the solvation shells structural properties, such as the angle distributions and the CNs. As both PC and Na^+ promotes local disorder in the electrolyte, as well as promoting HCE features, local heterogeneity might be essential for HCEs.

7. Outlook

Looking towards the future, there are several possible follow-up studies on the transport mechanism in HCEs. The average potentials studied in **Paper V** are all similar for the same solvents, but the residence times differ substantially, indicating that the exchange processes might not be thermally driven, *i.e.*, the exchanges do not necessarily occur because the solvent suddenly gained enough kinetic energy to overcome the potential barrier. Instead, it might be fluctuations in the potential barrier that drives the exchange. Thus, it would be the second solvation shell that facilitates exchanges, which is also indicated by the associative exchange process being more common, and that several attempt of entering the solvation shell is often seen before a successful associative exchange.

The potential barriers could also be analysed using Kramer's escape formalism [166], or by making an analogy with quantum tunnelling phenomenon. Both approaches should give insight into if it is the thermal motion of the solvent molecule inside the first solvation shell, or the fluctuations of the potential barrier, that drives the exchange processes.

Moreover, to directly investigate desolvation phenomena, the local electrolyte structure and dynamics should be studied in the presence of an electrode, or the SEI/CEI. This could either be done by explicitly simulating the electrolyte on one of these surfaces, or implicitly – smaller AIMD simulations of a single cation/anion/solvent on a surface could be used to extract the force on the species, as a function of distance from the surface. Once this is done for all species, a potential, reflecting the effects of the surface, could be added to an MD simulation.

Experimental studies on the CN and SN are often relegated to looking at averages of these quantities – but the majority of computational studies have full access to the distribution of these quantities, revealing details that might be difficult, or even impossible, for conventional experimental techniques to uncover. The computationally observed disorder in HCE might, however, be connected with the entropy of the electrolyte, which should be a measurable property. But, care must be taken when comparing computational and experimental results – especially as the terms CN and SN are often used interchangeably. Computational studies often look at the number of atoms in the solvation shell, by integrating the partial atomic RDFs, while in IR/Raman studies it can be hard to discern if it is the number of atoms, a specific functional group, or the number of solvents/anions in the solvation shell, or simply the amount of free solvents/anions, that is measured. The experimental and computational

methods should, and sometimes must, be used to complement each other – revealing a deeper and truer picture of the electrolyte. The structural studies of electrolytes should also move beyond the first solvation shell, locating all connected structures. This is especially important in HCE, as ionic aggregates are thought to play a crucial role.

The importance of disorder, or local heterogeneity, for the electrolyte properties could also be further studied by selecting salts and solvents which should promote higher disorder. For instance, by comparing potassium-ion battery electrolytes with LIB and SIB electrolytes, or by choosing anions or solvents with several possible coordination modes – such as displayed by PC – which might promote fast kinetics and the transport properties observed in HCE, thus enabling a rational design choice in the development of new electrolytes.

8. Acknowledgements

Starting with my supervisor Professor Patrik Johansson: Thank you for the freedom and opportunities you've given me during these years – I've grown more than I expected. Especially in muscle mass, who would have thought!

Moving on to Professor Aleksandar Matic, thank you for managing (K)MF through wisdom and humor. Then we have (K)MF. Where do I even start with this one. Through these years I've met, gotten to know, and made friends with people from all over the world – truly an amazing experience. I guess this is where I have to decide if I'm going to start naming all the people – risking forgetting someone. So… Nope! But, of course, Simon Lindberg, whom I've shared office with during these years, travelled with to Japan and South Africa, laughed, argued with and shared ups and downs, can't go unnoticed. YOU KNOW THAT I WON THE BET, AND YOU OWE ME A BOTTLE OF EXPENSIVE CHAMPAGNE. I'll hold up my end of the bargain, we will consume the bottle together. Seriously though, thank you for sharing this time with me.

A special thanks to Andreas Ask, Simon Lindberg, Matthew Sadd, Rasmus Andersson and Roza Bouchal for helping me proofread the thesis. Even though Matt removed all the jokes. You should have seen the first draft, honestly, it was hilarious! I've heard Simon is saving some of the best jokes for his own thesis.

I want to thank the Swedish Energy Agency, who has funded these projects though "Batterifondsprogrammet": "Next Generation Batteries" (#37671-1) and "Highly Concentrated Electrolytes" (#39909-1). I would also like to acknowledge financial support from the EU H2020 NAIADES project (LCE10-2014, #646433), and gratefully acknowledge the computational resources provided by the Swedish National Infrastructure for Computing (SNIC) at Chalmers Centre for Computational Science and Engineering (C3SE).

Finally, I must thank my friends and family, for always being there, for the laughs, and the support when I needed it the most.

References

[1] K. Ozawa, “Lithium-ion rechargeable batteries with $LiCoO_2$ and carbon electrodes: the $LiCoO_2$/C system,” *Solid State Ionics*, vol. 69, no. 3–4, pp. 212–221, Aug. 1994.

[2] Y. Nishi, “Lithium ion secondary batteries; past 10 years and the future,” *J. Power Sources*, vol. 100, no. 1–2, pp. 101–106, Nov. 2001.

[3] M. Li, J. Lu, Z. Chen, and K. Amine, “30 Years of Lithium-Ion Batteries,” *Adv. Mater.*, vol. 30, no. 33, p. 1800561, Aug. 2018.

[4] R. Rapier, “Why China is Dominating Lithium-Ion Battery Production,” 2019.

[5] I. Tsiropoulos, D. Tarvydas, and N. Lebedeva, *Li-ion batteries for mobility and stationary storage applications, JRC Science for Policy Report, EU Commission.* 2018.

[6] C. Vaalma, D. Buchholz, M. Weil, and S. Passerini, “A cost and resource analysis of sodium-ion batteries,” *Nat. Rev. Mater.*, vol. 3, no. 4, p. 18013, Apr. 2018.

[7] N. T. Nassar, T. E. Graedel, and E. M. Harper, “By-product metals are technologically essential but have problematic supply,” *Sci. Adv.*, vol. 1, no. 3, p. e1400180, Apr. 2015.

[8] Amnesty International, “‘This is what we die for’ Human rights abuses in the Democratic Republic of the Congo power the global trade in cobalt,” *Amnesty International*, 2016.

[9] T. C. Frankel, “The Cobalt Pipeline.”. Available: https://www.washingtonpost.com/graphics/business/batteries/congo-cobalt-mining-for-lithium-ion-battery/??noredirect=on. [Accessed: 26-Aug-2018].

[10] S. J. Davis, K. Caldeira, and H. D. Matthews, “Future CO2 Emissions and Climate Change from Existing Energy Infrastructure,” *Science (80-.).*, vol. 329, no. 5997, pp. 1330–1333, Sep. 2010.

[11] International Energy Agency, *CO2 Emissions from Fuel Combustion 2017*, vol. 1. OECD, 2017.

[12] M. Crippa *et al.*, *Fossil CO2 and GHG emissions of all world countries - 2019 Report, EUR 29849 EN*. 2019.

[13] Q. Dai, J. C. Kelly, L. Gaines, and M. Wang, “Life Cycle Analysis of Lithium-Ion Batteries for Automotive Applications,” *Batteries*, vol. 5, no. 2, p. 48, Jun. 2019.

[14] M. Romare and L. Dahllöf, *The Life Cycle Energy Consumption and Greenhouse Gas Emissions from Lithium-Ion Batteries*, no. C. 2017.

[15] J. C. Kelly, Q. Dai, and M. Wang, “Globally regional life cycle analysis of automotive lithium-ion nickel manganese cobalt batteries,” *Mitig. Adapt. Strateg. Glob. Chang.*, Aug. 2019.

[16] E. Emilsson and L. Dahllöf, *Lithium-Ion Vehicle Battery Production*, no. C. 2019.

[17] O. Cann, “These are the top 10 emerging technologies of 2016,” 2016. Available: https://www.weforum.org/agenda/2016/06/top-10-emerging-technologies-2016/. [Accessed: 22-Aug-2018].

[18] J. Carbeck, “These next-generation batteries could end energy poverty,” 2016. Available: https://www.weforum.org/agenda/2016/06/next-generation-batteries. [Accessed: 22-Aug-2018].

[19] C. Schütter, S. Pohlmann, and A. Balducci, “Industrial Requirements of Materials for Electrical Double Layer Capacitors: Impact on Current and Future Applications,” *Adv. Energy Mater.*, vol. 9, no. 25, p. 1900334, Jul. 2019.

[20] Z. P. Cano *et al.*, “Batteries and fuel cells for emerging electric vehicle markets,” *Nat. Energy*, vol. 3, no. 4, pp. 279–289, Apr. 2018.

[21] A. Lajunen and T. Lipman, “Lifecycle cost assessment and carbon dioxide emissions of diesel, natural gas, hybrid electric, fuel cell hybrid and electric transit buses,” *Energy*, vol. 106, pp. 329–342, Jul. 2016.
[22] A. Ponrouch *et al.*, “Towards high energy density sodium ion batteries through electrolyte optimization,” *Energy Environ. Sci.*, vol. 6, no. 8, pp. 2361–2369, 2013.
[23] D. Larcher and J.-M. Tarascon, “Towards greener and more sustainable batteries for electrical energy storage,” *Nat. Chem.*, vol. 7, no. 1, pp. 19–29, Jan. 2015.
[24] D. Monti, A. Ponrouch, M. R. Palacín, and P. Johansson, “Towards safer sodium-ion batteries via organic solvent/ionic liquid based hybrid electrolytes,” *J. Power Sources*, vol. 324, pp. 712–721, 2016.
[25] A. Ponrouch, D. Monti, A. Boschin, B. Steen, P. Johansson, and M. R. Palacín, “Non-aqueous electrolytes for sodium-ion batteries,” *J. Mater. Chem. A*, vol. 3, no. 1, pp. 22–42, 2015.
[26] M. D. Slater, D. Kim, E. Lee, and C. S. Johnson, “Sodium-Ion Batteries,” *Adv. Funct. Mater.*, vol. 23, no. 8, pp. 947–958, Feb. 2013.
[27] C. Delmas, “Sodium and Sodium-Ion Batteries: 50 Years of Research,” *Adv. Energy Mater.*, vol. 8, no. 17, p. 1703137, Jun. 2018.
[28] Y. Yamada and A. Yamada, “Review-Super concentrated electrolytes for lithium batteries,” *J. Electrochem. Soc.*, vol. 162, no. 14, pp. A2406–A2423, 2015.
[29] Y. Yamada, J. Wang, S. Ko, E. Watanabe, and A. Yamada, “Advances and issues in developing salt-concentrated battery electrolytes,” *Nat. Energy*, vol. 4, no. 4, pp. 269–280, Mar. 2019.
[30] O. Borodin, J. Self, K. A. Persson, C. Wang, and K. Xu, “Uncharted Waters: Super-Concentrated Electrolytes,” *Joule*, vol. 4, no. 1, pp. 69–100, Jan. 2020.
[31] C.-X. Zu and H. Li, “Thermodynamic analysis on energy densities of batteries,” *Energy Environ. Sci.*, vol. 4, no. 8, p. 2614, 2011.
[32] H. Berg, *Batteries for Electric Vehicles - Materials and Electrochemistry*. Cambridge University Press, 2015.
[33] N. Nitta, F. Wu, J. T. Lee, and G. Yushin, “Li-ion battery materials: present and future,” *Mater. Today*, vol. 18, no. 5, pp. 252–264, Jun. 2015.
[34] J. Betz, G. Bieker, P. Meister, T. Placke, M. Winter, and R. Schmuch, “Theoretical versus Practical Energy: A Plea for More Transparency in the Energy Calculation of Different Rechargeable Battery Systems,” *Adv. Energy Mater.*, vol. 9, no. 6, p. 1803170, Feb. 2019.
[35] “The Nobel Prize in Chemistry 2019,” *Nobel Media AB 2020*, 2019. Available: https://www.nobelprize.org/prizes/chemistry/2019/summary/. [Accessed: 22-Feb-2020].
[36] M. S. Whittingham, “The hydrated intercalation complexes of the layered disulfides,” *Mater. Res. Bull.*, vol. 9, no. 12, pp. 1681–1689, Dec. 1974.
[37] K. Mizushima, P. C. Jones, P. J. Wiseman, and J. B. Goodenough, “LixCoO$_2$ (0<x<-1): A new cathode material for batteries of high energy density,” *Mater. Res. Bull.*, vol. 15, no. 6, pp. 783–789, Jun. 1980.
[38] M. Armand, *Materials for Advanced Batteries*. Springer US, 1980.
[39] H. Zhang *et al.*, “From Solid-Solution Electrodes and the Rocking-Chair Concept to Today’s Batteries,” *Angew. Chemie Int. Ed.*, vol. 59, no. 2, pp. 534–538, Jan. 2020.
[40] A. Yoshino, “The birth of the lithium-ion battery,” *Angew. Chemie - Int. Ed.*, vol. 51, no. 24, pp. 5798–5800, 2012.
[41] D. Guyomard and J. M. Tarascon, “Rechargeable $Li_{1+x}Mn_2O_4$/Carbon Cells with a New Electrolyte Composition,” *J. Electrochem. Soc.*, vol. 140, no. 11, p. 3071, 1993.
[42] E. Peled, “The Electrochemical Behavior of Alkali and Alkaline Earth Metals in

Nonaqueous Battery Systems—The Solid Electrolyte Interphase Model," *J. Electrochem. Soc.*, vol. 126, no. 12, p. 2047, 1979.
[43] R. Fong, U. von Sacken, and J. R. Dahn, "Studies of Lithium Intercalation into Carbons Using Nonaqueous Electrochemical Cells," *J. Electrochem. Soc.*, vol. 137, no. 7, p. 2009, 1990.
[44] E. Peled and S. Menkin, "Review—SEI: Past, Present and Future," *J. Electrochem. Soc.*, vol. 164, no. 7, pp. A1703–A1719, 2017.
[45] J. W. Choi and D. Aurbach, "Promise and reality of post-lithium-ion batteries with high energy densities," *Nat. Rev. Mater.*, vol. 1, no. 4, p. 16013, Apr. 2016.
[46] J.-M. Tarascon and M. Armand, "Issues and challenges facing rechargeable lithium batteries," *Nature*, vol. 414, no. 6861, pp. 359–367, Nov. 2001.
[47] T. B. Reddy, *Linden's handbook of batteries*. McGraw-Hill, 2011.
[48] M. M. B. Schott, A. Püttner, "The Market for Battery Electric Vehicles," in *Advances in Battery Technology for Electrical Vehicles*, Woodhead Publisher, 2015.
[49] K. Sawai, Y. Iwakoshi, and T. Ohzuku, "Carbon materials for lithium-ion (shuttlecock) cells," *Solid State Ionics*, vol. 69, no. 3–4, pp. 273–283, 1994.
[50] T. Ohzuku, A. Ueda, and N. Yamamoto, "Zero-Strain Insertion Material of Li $Li_{1/3}Ti_{5/3}O_4$ for Rechargeable Lithium Cells," *J. Electrochem. Soc.*, vol. 142, no. 5, pp. 1431–1435, 1995.
[51] E. Ferg, R. J. Gummow, A. Kock, and M. M. Thackeray, "Spinel Anodes for Lithium-Ion Batteries," *J. Electrochem. Soc.*, vol. 141, no. 11, p. L147, 1994.
[52] K. M. Colbow, J. R. Dahn, and R. R. Haering, "Structure and electrochemistry of the spinel oxides $LiTi_2O_4$ and $Li_{43}Ti_{53}O_4$," *J. Power Sources*, vol. 26, no. 3–4, pp. 397–402, May 1989.
[53] A. Manthiram, J. C. Knight, S.-T. Myung, S.-M. Oh, and Y.-K. Sun, "Nickel-Rich and Lithium-Rich Layered Oxide Cathodes: Progress and Perspectives," *Adv. Energy Mater.*, vol. 6, no. 1, p. 1501010, Jan. 2016.
[54] G. Zubi, R. Dufo-López, M. Carvalho, and G. Pasaoglu, "The lithium-ion battery: State of the art and future perspectives," *Renew. Sustain. Energy Rev.*, vol. 89, no. October 2017, pp. 292–308, Jun. 2018.
[55] M. H. Rossouw, D. C. Liles, and M. M. Thackeray, "Synthesis and Structural Characterization of a Novel Layered Lithium Manganese Oxide, $Li_{0.36}Mn_{0.91}O_2$, and Its Lithiated Derivative, $Li_{1.09}Mn_{0.91}O_2$," *J. Solid State Chem.*, vol. 104, no. 2, pp. 464–466, Jun. 1993.
[56] A. K. Padhi, K. S. Nanjundaswamy, and J. B. Goodenough, "Phospho-olivines as Positive-Electrode Materials for Rechargeable Lithium Batteries," *J. Electrochem. Soc.*, vol. 144, no. 4, p. 1188, 1997.
[57] J. Janek and W. G. Zeier, "A solid future for battery development," *Nat. Energy*, vol. 1, no. 9, p. 16141, Sep. 2016.
[58] T. Placke, R. Kloepsch, S. Dühnen, and M. Winter, "Lithium ion, lithium metal, and alternative rechargeable battery technologies: the odyssey for high energy density," *J. Solid State Electrochem.*, vol. 21, no. 7, pp. 1939–1964, Jul. 2017.
[59] A. Manthiram, Y. Fu, S.-H. Chung, C. Zu, and Y.-S. Su, "Rechargeable Lithium–Sulfur Batteries," *Chem. Rev.*, vol. 114, no. 23, pp. 11751–11787, Dec. 2014.
[60] K. M. Abraham, "A Polymer Electrolyte-Based Rechargeable Lithium/Oxygen Battery," *J. Electrochem. Soc.*, vol. 143, no. 1, p. 1, 1996.
[61] D. Aurbach, B. D. McCloskey, L. F. Nazar, and P. G. Bruce, "Advances in understanding mechanisms underpinning lithium–air batteries," *Nat. Energy*, vol. 1, no. 9, p. 16128, Sep. 2016.
[62] P. G. Bruce, S. A. Freunberger, L. J. Hardwick, and J.-M. Tarascon, "Li–O_2 and Li–S

batteries with high energy storage," *Nat. Mater.*, vol. 11, no. 1, pp. 19–29, Jan. 2012.
[63] A. Ponrouch, J. Bitenc, R. Dominko, N. Lindahl, P. Johansson, and M. R. Palacin, "Multivalent rechargeable batteries," *Energy Storage Mater.*, vol. 20, no. April, pp. 253–262, Jul. 2019.
[64] I. Shterenberg, M. Salama, Y. Gofer, E. Levi, and D. Aurbach, "The challenge of developing rechargeable magnesium batteries," *MRS Bull.*, vol. 39, no. 5, pp. 453–460, May 2014.
[65] A. Ponrouch, C. Frontera, F. Bardé, and M. R. Palacín, "Towards a calcium-based rechargeable battery," *Nat. Mater.*, vol. 15, no. 2, pp. 169–172, Feb. 2016.
[66] R. Attias, M. Salama, B. Hirsch, Y. Goffer, and D. Aurbach, "Anode-Electrolyte Interfaces in Secondary Magnesium Batteries," *Joule*, vol. 3, no. 1, pp. 27–52, Jan. 2019.
[67] D. Aurbach, "The Electrochemical Behavior of Calcium Electrodes in a Few Organic Electrolytes," *J. Electrochem. Soc.*, vol. 138, no. 12, p. 3536, 1991.
[68] J. Verne, *Vingt mille lieurs sous les mers*. 1870.
[69] T. R. Jow, L. W. Shacklette, M. Maxfield, and D. Vernick, "Role of Conductive Polymers in Alkali-Metal Secondary Electrodes.," *Proc. - Electrochem. Soc.*, vol. 87–1, pp. 314–324, 1987.
[70] M. M. Doeff, Y. Ma, S. J. Visco, and D. L. C. Jonghe, "Electrochemical Insertion of Sodium into Carbon," *J. Electrochem. Soc.*, vol. 140, no. 12, p. L169, Aug. 1993.
[71] A. Bauer, J. Song, S. Vail, W. Pan, J. Barker, and Y. Lu, "The Scale-up and Commercialization of Nonaqueous Na-Ion Battery Technologies," *Adv. Energy Mater.*, vol. 8, no. 17, pp. 1–13, 2018.
[72] K. Kubota and S. Komaba, "Review—Practical Issues and Future Perspective for Na-Ion Batteries," *J. Electrochem. Soc.*, vol. 162, no. 14, pp. A2538–A2550, 2015.
[73] H. Pan, Y.-S. Hu, and L. Chen, "Room-temperature stationary sodium-ion batteries for large-scale electric energy storage," *Energy Environ. Sci.*, vol. 6, no. 8, p. 2338, 2013.
[74] G.-C. Ri, C.-J. Yu, J.-S. Kim, S.-N. Hong, U.-G. Jong, and M.-H. Ri, "First-principles study of ternary graphite compounds cointercalated with alkali atoms (Li, Na, and K) and alkylamines towards alkali ion battery applications," *J. Power Sources*, vol. 324, pp. 758–765, Aug. 2016.
[75] Y. Liu *et al.*, "In situ transmission electron microscopy study of electrochemical sodiation and potassiation of carbon nanofibers," *Nano Lett.*, vol. 14, no. 6, pp. 3445–3452, 2014.
[76] S. Y. Hong, Y. Kim, Y. Park, A. Choi, N. S. Choi, and K. T. Lee, "Charge carriers in rechargeable batteries: Na ions vs. Li ions," *Energy Environ. Sci.*, vol. 6, no. 7, pp. 2067–2081, 2013.
[77] B. Jache and P. Adelhelm, "Use of Graphite as a Highly Reversible Electrode with Superior Cycle Life for Sodium-Ion Batteries by Making Use of Co-Intercalation Phenomena," *Angew. Chemie Int. Ed.*, vol. 53, no. 38, pp. 10169–10173, Sep. 2014.
[78] P. Senguttuvan, G. Rousse, V. Seznec, J. M. Tarascon, and M. R. Palacín, "$Na_2Ti_3O_7$: Lowest voltage ever reported oxide insertion electrode for sodium ion batteries," *Chem. Mater.*, vol. 23, no. 18, pp. 4109–4111, 2011.
[79] X. Dou *et al.*, "Hard carbons for sodium-ion batteries: Structure, analysis, sustainability, and electrochemistry," *Mater. Today*, vol. 23, no. March, pp. 87–104, Mar. 2019.
[80] D. A. Stevens and J. R. Dahn, "High Capacity Anode Materials for Rechargeable Sodium-Ion Batteries," *J. Electrochem. Soc.*, vol. 147, no. 4, p. 1271, 2000.
[81] J. Barker, M. Y. Saidi, and J. L. Swoyer, "A Sodium-Ion Cell Based on the Fluorophosphate Compound $NaVPO_4F$," *Electrochem. Solid-State Lett.*, vol. 6, no. 1,

p. A1, 2003.
[82] R. Gover, A. Bryan, P. Burns, and J. Barker, “The electrochemical insertion properties of sodium vanadium fluorophosphate, $Na_3V_2(PO_4)_2F_3$,” *Solid State Ionics*, vol. 177, no. 17–18, pp. 1495–1500, Jul. 2006.
[83] N. Ortiz-Vitoriano, N. E. Drewett, E. Gonzalo, and T. Rojo, “High performance manganese-based layered oxide cathodes: overcoming the challenges of sodium ion batteries,” *Energy Environ. Sci.*, vol. 10, no. 5, pp. 1051–1074, 2017.
[84] I. Hasa, S. Passerini, and J. Hassoun, “Characteristics of an ionic liquid electrolyte for sodium-ion batteries,” *J. Power Sources*, vol. 303, pp. 203–207, Jan. 2016.
[85] H. Liu, J. Xu, C. Ma, and Y. S. Meng, “A new O_3-type layered oxide cathode with high energy/power density for rechargeable Na batteries,” *Chem. Commun.*, vol. 51, no. 22, pp. 4693–4696, 2015.
[86] S. S. Zhang, “A review on electrolyte additives for lithium-ion batteries,” *J. Power Sources*, vol. 162, no. 2, pp. 1379–1394, Nov. 2006.
[87] K. Xu, “Electrolytes and interphases in Li-ion batteries and beyond,” *Chem. Rev.*, vol. 114, no. 23, pp. 11503–11618, 2014.
[88] K. Xu, Y. Lam, S. S. Zhang, T. R. Jow, and T. B. Curtis, “Solvation sheath of Li^+ in nonaqueous electrolytes and its implication of graphite/electrolyte interface chemistry,” *J. Phys. Chem. C*, vol. 111, no. 20, pp. 7411–7421, 2007.
[89] K. Xu, “‘Charge-Transfer’ Process at Graphite/Electrolyte Interface and the Solvation Sheath Structure of Li^+ in Nonaqueous Electrolytes,” *J. Electrochem. Soc.*, vol. 154, no. 3, p. A162, 2007.
[90] J. O. Bockris and A. K. N. Reddy, *Modern Electrochemistry 1 - Ionics*, Second edition. Plenum Press, 1998.
[91] J. L. Allen, O. Borodin, D. M. Seo, and W. A. Henderson, “Combined quantum chemical/Raman spectroscopic analyses of Li^+ cation solvation: Cyclic carbonate solvents - Ethylene carbonate and propylene carbonate,” *J. Power Sources*, vol. 267, pp. 821–830, 2014.
[92] R. M. Fuoss and L. Onsager, “Conductance of Unassociated Electrolytes.,” *J. Phys. Chem.*, vol. 61, no. 5, pp. 668–682, May 1957.
[93] J. Newman and K. E. Thomas-Alyea, *Electrochemical Systems*. John Wiley & Sons, Ltd, 2012.
[94] M. Forsyth *et al.*, “Novel Na^+ Ion Diffusion Mechanism in Mixed Organic–Inorganic Ionic Liquid Electrolyte Leading to High Na^+ Transference Number and Stable, High Rate Electrochemical Cycling of Sodium Cells.,” *J. Phys. Chem. C*, vol. 120, no. 8, pp. 4276–4286, Mar. 2016.
[95] F. Chen and M. Forsyth, “Elucidation of transport mechanism and enhanced alkali ion transference numbers in mixed alkali metal–organic ionic molten salts,” *Phys. Chem. Chem. Phys.*, vol. 18, no. 28, pp. 19336–19344, 2016.
[96] S. A. Krachkovskiy, J. D. Bazak, S. Fraser, I. C. Halalay, and G. R. Goward, “Determination of Mass Transfer Parameters and Ionic Association of $LiPF_6$: Organic Carbonates Solutions,” *J. Electrochem. Soc.*, vol. 164, no. 4, pp. A912–A916, 2017.
[97] A. V. Cresce *et al.*, “Solvation behavior of carbonate-based electrolytes in sodium ion batteries,” *Phys. Chem. Chem. Phys.*, vol. 19, no. 1, pp. 574–586, 2017.
[98] D. M. Seo *et al.*, “Electrolyte Solvation and Ionic Association III. Acetonitrile-Lithium Salt Mixtures-Transport Properties,” *J. Electrochem. Soc.*, vol. 160, no. 8, pp. A1061–A1070, May 2013.
[99] J. Wahlers, K. D. Fulfer, D. P. Harding, D. G. Kuroda, R. Kumar, and R. Jorn, “Solvation Structure and Concentration in Glyme-Based Sodium Electrolytes: A Combined Spectroscopic and Computational Study,” *J. Phys. Chem. C*, vol. 120, no.

32, pp. 17949–17959, Aug. 2016.
[100] K. Dokko *et al.*, “Direct Evidence for Li Ion Hopping Conduction in Highly Concentrated Sulfolane-Based Liquid Electrolytes,” *J. Phys. Chem. B*, vol. 122, no. 47, pp. 10736–10745, Nov. 2018.
[101] O. Borodin *et al.*, “Liquid Structure with Nano-Heterogeneity Promotes Cationic Transport in Concentrated Electrolytes,” *ACS Nano*, vol. 11, no. 10, pp. 10462–10471, 2017.
[102] B. Bagchi and B. Jana, “Solvation dynamics in dipolar liquids,” *Chem. Soc. Rev.*, vol. 39, no. 6, pp. 1936–1954, 2010.
[103] K. Oldiges *et al.*, “Understanding transport mechanisms in ionic liquid/carbonate solvent electrolyte blends,” *Phys. Chem. Chem. Phys.*, vol. 20, no. 24, pp. 16579–16591, 2018.
[104] O. Borodin and G. D. Smith, “LiTFSI Structure and Transport in Ethylene Carbonate from Molecular Dynamics Simulations,” *J. Phys. Chem. B*, vol. 110, no. 10, pp. 4971–4977, Mar. 2006.
[105] J. Self, K. D. Fong, and K. A. Persson, “Transport in Superconcentrated $LiPF_6$ and $LiBF_4$/Propylene Carbonate Electrolytes,” *ACS Energy Lett.*, pp. 2843–2849, Nov. 2019.
[106] M. Okoshi, C.-P. Chou, and H. Nakai, “Theoretical Analysis of Carrier Ion Diffusion in Superconcentrated Electrolyte Solutions for Sodium-Ion Batteries,” *J. Phys. Chem. B*, vol. 122, no. 9, pp. 2600–2609, Mar. 2018.
[107] O. Borodin *et al.*, “Insights into the Structure and Transport of the Lithium, Sodium, Magnesium, and Zinc Bis(trifluoromethansulfonyl)imide Salts in Ionic Liquids,” *J. Phys. Chem. C*, vol. 122, no. 35, pp. 20108–20121, Sep. 2018.
[108] S. Koneshan, J. C. Rasaiah, R. M. Lynden-Bell, and S. H. Lee, “Solvent Structure, Dynamics, and Ion Mobility in Aqueous Solutions at 25°C,” *J. Phys. Chem. B*, vol. 102, no. 21, pp. 4193–4204, May 1998.
[109] S. Raugei and M. L. Klein, “An ab initio study of water molecules in the bromide ion solvation shell,” *J. Chem. Phys.*, vol. 116, no. 1, p. 196, 2002.
[110] J. M. Heuft and E. J. Meijer, “Density functional theory based molecular-dynamics study of aqueous chloride solvation,” *J. Chem. Phys.*, vol. 119, no. 22, pp. 11788–11791, Dec. 2003.
[111] V. S. Smirnov and S. A. Kislenko, “Effect of Solvents on the Behavior of Lithium and Superoxide Ions in Lithium-Oxygen Battery Electrolytes,” *ChemPhysChem*, vol. 19, no. 1, pp. 75–81, Jan. 2018.
[112] J. O. Besenhard and H. P. Fritz, “The Electrochemistry of Black Carbons,” *Angew. Chemie Int. Ed. English*, vol. 22, no. 12, pp. 950–975, Dec. 1983.
[113] M. Arakawa and J.-I. Yamaki, “The cathodic decomposition of propylene carbonate in lithium batteries,” *J. Electroanal. Chem. Interfacial Electrochem.*, vol. 219, no. 1–2, pp. 273–280, Mar. 1987.
[114] J. O. Besenhard and H. P. Fritz, “Cathodic reduction of graphite in organic solutions of alkali and NR_4^+ salts,” *J. Electroanal. Chem. Interfacial Electrochem.*, vol. 53, no. 2, pp. 329–333, Jun. 1974.
[115] G. Eichinger, “Cathodic decomposition reactions of propylene carbonate,” *J. Electroanal. Chem. Interfacial Electrochem.*, vol. 74, no. 2, pp. 183–193, Dec. 1976.
[116] A. N. Dey and B. P. Sullivan, “The Electrochemical Decomposition of Propylene Carbonate on Graphite,” *J. Electrochem. Soc.*, vol. 117, no. 2, p. 222, 1970.
[117] K. Xu, “Nonaqueous Liquid Electrolytes for Lithium-Based Rechargeable Batteries,” *Chem. Rev.*, vol. 104, no. 10, pp. 4303–4418, Oct. 2004.
[118] G. H. Newman, R. W. Francis, L. H. Gaines, and B. M. L. Rao, “Technica Hazard

Investigations of $LiClO_4$ / Dioxolane Electrolyte," *J. Electrochem. Soc.*, vol. 127, no. 9, pp. 2025–2027, 1980.
[119] R. Jasinski and S. Carroll, "Thermal Stability of a Propylene Carbonate Electrolyte," *J. Electrochem. Soc.*, vol. 117, no. 2, p. 218, 1970.
[120] F. Kita, A. Kawakami, J. Nie, T. Sonoda, and H. Kobayashi, "On the characteristics of electrolytes with new lithium imide salts," *J. Power Sources*, vol. 68, no. 2, pp. 307–310, Oct. 1997.
[121] Y. Yamada *et al.*, "Unusual Stability of Acetonitrile-Based Superconcentrated Electrolytes for Fast-Charging Lithium-Ion Batteries," *J. Am. Chem. Soc.*, vol. 136, no. 13, pp. 5039–5046, Apr. 2014.
[122] Y. Yamada, M. Yaegashi, T. Abe, and A. Yamada, "A superconcentrated ether electrolyte for fast-charging Li-ion batteries," *Chem. Commun.*, vol. 49, no. 95, p. 11194, 2013.
[123] R. Petibon, C. P. Aiken, L. Ma, D. Xiong, and J. R. Dahn, "The use of ethyl acetate as a sole solvent in highly concentrated electrolyte for Li-ion batteries," *Electrochim. Acta*, vol. 154, pp. 287–293, 2015.
[124] K. Yoshida *et al.*, "Oxidative-Stability Enhancement and Charge Transport Mechanism in Glyme–Lithium Salt Equimolar Complexes," *J. Am. Chem. Soc.*, vol. 133, no. 33, pp. 13121–13129, Aug. 2011.
[125] J. Wang, Y. Yamada, K. Sodeyama, C. H. Chiang, Y. Tateyama, and A. Yamada, "Superconcentrated electrolytes for a high-voltage lithium-ion battery," *Nat. Commun.*, vol. 7, no. 1, p. 12032, Nov. 2016.
[126] K. Matsumoto, K. Inoue, K. Nakahara, R. Yuge, T. Noguchi, and K. Utsugi, "Suppression of aluminum corrosion by using high concentration LiTFSI electrolyte," *J. Power Sources*, vol. 231, pp. 234–238, Jun. 2013.
[127] L. Suo, Y.-S. Hu, H. Li, M. Armand, and L. Chen, "A new class of Solvent-in-Salt electrolyte for high-energy rechargeable metallic lithium batteries," *Nat. Commun.*, vol. 4, no. 1, p. 1481, Jun. 2013.
[128] K. Dokko *et al.*, "Solvate Ionic Liquid Electrolyte for Li–S Batteries," *J. Electrochem. Soc.*, vol. 160, no. 8, pp. A1304–A1310, Jun. 2013.
[129] S. Jiao *et al.*, "Stable cycling of high-voltage lithium metal batteries in ether electrolytes," *Nat. Energy*, vol. 3, no. 9, pp. 739–746, Sep. 2018.
[130] S.-K. Jeong *et al.*, "Suppression of dendritic lithium formation by using concentrated electrolyte solutions," *Electrochem. commun.*, vol. 10, no. 4, pp. 635–638, Apr. 2008.
[131] J. Qian *et al.*, "High rate and stable cycling of lithium metal anode," *Nat. Commun.*, vol. 6, no. 1, p. 6362, May 2015.
[132] J. Wang *et al.*, "Fire-extinguishing organic electrolytes for safe batteries," *Nat. Energy*, vol. 3, no. 1, pp. 22–29, Jan. 2018.
[133] Z. Zeng *et al.*, "Non-flammable electrolytes with high salt-to-solvent ratios for Li-ion and Li-metal batteries," *Nat. Energy*, vol. 3, no. 8, pp. 674–681, Aug. 2018.
[134] D. Bedrov, O. Borodin, Z. Li, and G. D. Smith, "Influence of Polarization on Structural, Thermodynamic, and Dynamic Properties of Ionic Liquids Obtained from Molecular Dynamics Simulations," *J. Phys. Chem. B*, vol. 114, no. 15, pp. 4984–4997, Apr. 2010.
[135] J. B. Foresman and Æ. Firsch, *Exploring Chemistry with Electronic Structure Methods*, Third Edition. Gaussian Inc, 2015.
[136] L. Goerigk and S. Grimme, "A thorough benchmark of density functional methods for general main group thermochemistry, kinetics, and noncovalent interactions," *Phys. Chem. Chem. Phys.*, vol. 13, no. 14, p. 6670, 2011.
[137] J. J. Sakurai and J. Napolitano, *Modern Quantum Mechanics*, Second Edition. Pearson,

2011.
[138] P. A. M. Dirac, “Quantum mechanics of many-electron systems,” *Proc. R. Soc. London. Ser. A, Contain. Pap. a Math. Phys. Character*, vol. 123, no. 792, pp. 714–733, Apr. 1929.
[139] R. P. Feynman, “Simulating physics with computers,” *Int. J. Theor. Phys.*, vol. 21, no. 467, 1982.
[140] M. A. Nielsen and I. I. Chung, *Quantum Computation and Quantum Information*. Cambridge University Press, 2010.
[141] D. R. Hartree and W. Hartree, “Self-consistent field, with exchange, for beryllium,” *Proc. R. Soc. London. Ser. A - Math. Phys. Sci.*, vol. 150, no. 869, pp. 9–33, May 1935.
[142] J. M. Thijssen, *Computational Physics*, Second Edition. Cambridge University Press, 2007.
[143] J. J. P. Stewart, “Optimization of parameters for semiempirical methods VI: more modifications to the NDDO approximations and re-optimization of parameters,” *J. Mol. Model.*, vol. 19, no. 1, pp. 1–32, Jan. 2013.
[144] J. A. Pople, D. P. Santry, and G. A. Segal, “Approximate Self-Consistent Molecular Orbital Theory. I. Invariant Procedures,” *J. Chem. Phys.*, vol. 43, no. 10, pp. S129–S135, 1965.
[145] P. Hohenberg and W. Kohn, “Inhomogeneous Electron Gas,” *Phys. Rev.*, vol. 136, no. 3B, pp. B864–B871, Nov. 1964.
[146] W. Kohn and L. J. Sham, “Self-Consistent Equations Including Exchange and Correlation Effects,” *Phys. Rev.*, vol. 140, no. 4A, pp. A1133–A1138, Nov. 1965.
[147] J. P. Perdew, “Jacob’s ladder of density functional approximations for the exchange-correlation energy,” *AIP Conf. Proc.*, vol. 577, no. 2001, pp. 1–20, 2001.
[148] Y. Zhao and D. G. Truhlar, “The M06 suite of density functionals for main group thermochemistry, thermochemical kinetics, noncovalent interactions, excited states, and transition elements: two new functionals and systematic testing of four M06-class functionals and 12 other function,” *Theor. Chem. Acc.*, vol. 120, no. 1–3, pp. 215–241, May 2008.
[149] E. Jónsson and P. Johansson, “Modern battery electrolytes: Ion–ion interactions in Li^+/Na^+ conductors from DFT calculations,” *Phys. Chem. Chem. Phys.*, vol. 14, no. 30, p. 10774, 2012.
[150] J. P. Perdew, K. Burke, and M. Ernzerhof, “Generalized gradient approximation made simple,” *Phys. Rev. Lett.*, vol. 77, no. 18, pp. 3865–3868, 1996.
[151] R. P. Feynman, “Forces in Molecules,” *Phys. Rev.*, vol. 56, no. 4, pp. 340–343, Aug. 1939.
[152] R. Car and M. Parrinello, “Unified Approach for Molecular Dynamics and Density-Functional Theory,” *Phys. Rev. Lett.*, vol. 55, no. 22, pp. 2471–2474, Nov. 1985.
[153] H. Goldstein, C. Poole, and J. Safko, *Classical Mechanics - Third edition*. Pearson; Addison Wesley, 2002.
[154] H. B. Schlegel, “Geometry optimization,” *Wiley Interdiscip. Rev. Comput. Mol. Sci.*, vol. 1, no. 5, pp. 790–809, 2011.
[155] H. B. Schlegel, “Optimization of equalibrium geometries and transition structures,” *Adv. Chem. Phys.*, vol. 67, no. 2, p. 249, 1987.
[156] J. W. Ochterski and D. Ph, “Thermochemistry in Gaussian,” *Gaussian Inc Pittsburgh PA*, vol. 264, no. 1, pp. 1–19, 2000.
[157] S. K. Jeong, M. Inaba, Y. Iriyama, T. Abe, and Z. Ogumi, “Electrochemical intercalation of lithium ion within graphite from propylene carbonate solutions,” *Electrochem. Solid-State Lett.*, vol. 6, no. 1, pp. 15–17, 2003.

[158] K. L. Browning, R. L. Sacci, and G. M. Veith, "Energetics of Na^+ Transport through the Electrode/Cathode Interface in Single Solvent Electrolytes," *J. Electrochem. Soc.*, vol. 164, no. 4, pp. A580–A586, Jan. 2017.
[159] G. Kamath *et al.*, "In Silico Based Rank-Order Determination and Experiments on Nonaqueous Electrolytes for Sodium Ion Battery Applications," *J. Phys. Chem. C*, vol. 118, no. 25, pp. 13406–13416, Jun. 2014.
[160] D. Spångberg and K. Hermansson, "The solvation of Li^+ and Na^+ in acetonitrile from ab initio-derived many-body ion-solvent potentials," *Chem. Phys.*, vol. 300, no. 1–3, pp. 165–176, 2004.
[161] E. Cabaleiro-Lago and M. A. Rios, "An intermolecular potential function for Na^+-acetonitrile obtained from ab initio calculations. Application to liquid simulations," *Chem. Phys.*, vol. 236, pp. 235–242, 1998.
[162] M. Okoshi, Y. Yamada, A. Yamada, and H. Nakai, "Theoretical Analysis on De-Solvation of Lithium, Sodium, and Magnesium Cations to Organic Electrolyte Solvents," *J. Electrochem. Soc.*, vol. 160, no. 11, pp. A2160–A2165, Oct. 2013.
[163] M. Okoshi, Y. Yamada, S. Komaba, A. Yamada, and H. Nakai, "Theoretical Analysis of Interactions between Potassium Ions and Organic Electrolyte Solvents: A Comparison with Lithium, Sodium, and Magnesium Ions," *J. Electrochem. Soc.*, vol. 164, no. 2, pp. A54–A60, Dec. 2017.
[164] S. Chen, J. Ishii, S. Horiuchi, M. Yoshizawa-Fujita, and E. I. Izgorodina, "Difference in chemical bonding between lithium and sodium salts: influence of covalency on their solubility," *Phys. Chem. Chem. Phys.*, vol. 19, no. 26, pp. 17366–17372, 2017.
[165] S. De, A. Boda, and S. M. Ali, "Preferential interaction of charged alkali metal ions (guest) within a narrow cavity of cyclic crown ethers (neutral host): A quantum chemical investigation," *J. Mol. Struct. THEOCHEM*, vol. 941, no. 1–3, pp. 90–101, Feb. 2010.
[166] V. I. Mel'nikov, "The Kramers problem: Fifty years of development," *Phys. Rep.*, vol. 209, no. 1–2, pp. 1–71, Dec. 1991.